https://doi.org/10.5194/egusphere-2025-6352
Preprint. Discussion started: 10 March 2026

EnviFlux (v1.0): a simplified surface flux inversion tool based on four-dimensional variational data assimilation (4D-Var)

Ross N Bannister[1,2]

[1]Dept. of Meteorology, Univ. of Reading, Whiteknights Road, Earley Gate, Reading, RG6 6ET, UK
[2]National Centre for Earth Observation, Univ. of Leicester, UK

Correspondence: Ross N Bannister (r.n.bannister@reading.ac.uk)

Abstract. This paper introduces EnviFlux, which is a software tool (written in C++) to study the inverse problem of estimating the distribution of fluxes of a trace gas at the Earth's surface. This is done using a four-dimensional variational technique, which combines information from (i) synthetic observations of the trace gas spanning a defined time window, (ii) a transport model linking the initial concentration and surface fluxes to predictions of the observations, and (iii) a-priori information. The novelty of this system – compared to those that attempt to solve for real data – is in its relative simplicity and low cost, allowing new ideas to be assessed and understood quickly and cheaply. This is in line with many other developments in data assimilation that are often first explored using so-called "toy" systems. Part of this paper is to document this system, which is sufficiently complex to allow assimilation of in situ and total column amount (TCA) observation in arbitrary configurations, and has a flexible background error covariance model, but is simple enough to be run relatively quickly.

Another part of this paper uses EnviFlux to explore the effect of model error and observation bias on inferred surface fluxes in two example scenarios and with two observation types, namely surface in situ (SIS) and TCA. The first is a highly idealised case with a flux pair (a localised source and a localised sink), where no a-priori information concerning their positions is provided. It is found that model errors in the assimilation can severely affect the inferred flux positions and amounts, but observation biases do not affect the positions, but do affect the amounts. The second scenario is closer to a real-world example of methane flux estimates where an a-priori is refined with observations. The effect of model error is less than for the first scenario, but is still evident, and the observation biases affect the flux amounts. In both cases, the SIS observations allow a more accurate estimate of surface flux characteristics than the TCA observations, even though the experiments are setup to allow a fair comparison of the two.

The last part of the paper raises some research questions that EnviFlux could help address, and the appendices describe the particular background error covariance scheme used.

1 Introduction

A great potential of data assimilation is in its scope to infer hidden information that cannot be easily measured directly or accurately. The estimation of the rates of exchange of trace gases at the Earth's surface is one example that has important uses, e.g. in understanding and quantifying what processes and locations are responsible for the increasing concentrations of

https://doi.org/10.5194/egusphere-2025-6352
Preprint. Discussion started: 10 March 2026

greenhouse gases in the Earth's atmosphere. Example studies include those for CO_2 (Chevallier et al., 2005b; Feng et al., 2009), CH_4 (Fraser et al., 2013; Qu et al., 2021), N_2O (Hirsch et al., 2006; Thompson et al., 2019), and other trace gases (Jiang et al., 2013; An et al., 2012; Ma et al., 2021; Palmer et al., 2006; Gonzi et al., 2011). The method works by combining measurements of trace gas concentrations downstream of surface sources or sinks, with rules about how the air gets modified by the sources and sinks, and then how it is transported to the observation sites (this is usually in the form of a chemical transport model). This process is called "inverse modelling" or "top-down flux estimation" (Houweling et al., 2017) and has been applied using a number of techniques. These include direct inversions (using an explicit estimator formula) to infer the fluxes over a small number of large geographical regions (Gurney et al., 2002; Chandra et al., 2022), Markov chain Monte-Carlo (Lunt et al., 2019), regressions (Palmer et al., 2003), back-trajectories (An et al., 2012), fixed-lag Kalman smoothers (Zhuravlev et al., 2013), ensemble Kalman filters (Feng et al., 2009; Bisht et al., 2023; Pendergrass et al., 2023), and 4D-Var (Houweling et al., 1999; Chevallier et al., 2005b; Meirink et al., 2008b; Wilson et al., 2014).

Even the most carefully implemented inverse modelling studies have shortcomings owing to unknown or imperfectly modelled processes, unaccounted for errors, or incorrectly specified error covariances. One such issue is the influence of inevitable transport errors on the flux estimates, which has been the subject of numerous studies (Chevallier et al., 2010; Basu et al., 2018; Schuh et al., 2019; Munassar et al., 2023). In particular, Houweling et al. (2010) found that transport errors contributed to the uncertainty in CO_2 fluxes of $0.1\,\mathrm{PgCyr}^{-1}(10^6\mathrm{km}^2)^{-1}$ over land even though the model imperfections resulted in errors in predicted CO_2 column averages of just $0.5\,\mathrm{ppm}$ (comparable to the measurement error considered). Jiang et al. (2013) reported that for the estimate of CO fluxes, transport model errors can contribute to 5% of global emission errors, with larger values as the scale of interest gets smaller, becoming one and a half times the a-priori fluxes at the model grid level. Further, Chen et al. (2019) found different locations of CO_2 fluxes depending on the transport model used in the inversion. Another issue is the presence of biases (Chevallier et al., 2005a, 2010), which – whether in the model or in the observations – can contribute to large innovations, and hence to anomalous inferred fluxes.

These, and many other issues (see, e.g. the conclusions section of this paper), means that there is still a huge amount of research to be done to develop and refine inverse modelling techniques. Chemical transport models (CTM, and hence the whole inverse modelling procedures) are expensive to run (Agustí-Panareda et al., 2019), and so there is scope to explore some new ideas using low-cost simplified flux inversion systems that can be run repeatedly without the need for expensive high performance computers. This paper introduces a much simplified Environmental Flux inverse system "EnviFlux" that can be used to do low-cost experimentation around ideas related to such inverse problems. The software is designed to investigate the 4D-Var method of solving the the flux inversion problem inexpensively by running idealised twin experiments (as other authors have done in more complex and expensive systems, e.g. Chevallier et al. (2007); Basu et al. (2018); Yu et al. (2021); Voshtani et al. (2023). It is hoped that some lessons learned with this simplified system can be transferred to real-world (particularly 4D-Var-based) systems such as those used in Henze et al. (2007) (based on GEOS-Chem, Bey et al. (2001)), Chevallier et al. (2005b) (based on LMDZ, Hourdin and Armengaud (1999)), Meirink et al. (2008b) (based on TM5, Krol et al. (2005)), Wilson et al. (2014) (INVICAT, based on TOMCAT, Chipperfield (2006)), Hu et al. (2023) (based on WRF-Chem, Grell et al. (2005)),

https://doi.org/10.5194/egusphere-2025-6352
Preprint. Discussion started: 10 March 2026

and other models, and their developments. This paper demonstrates some findings from EnviFlux by studying the impact of model error and observation biases on the ability to infer the positions and magnitudes of surface fluxes of a generic trace gas.

The structure of this paper is as follows. Section 2 describes the basic set-up of the system, including the state vector, the computational grids, and the tracer transport scheme. Section 3 describes how the inverse problem is solved in the context of 4D-Var. Sections 4 and 5 provide demonstrations of the system, one with a example to estimate the position and magnitude of a source/sink pair in a "weakly Bayesian" (minimal a-priori information) context, and another with a more conventional Bayesian set-up to improve a given a-priori with observations. Section 6 summarises the findings, and poses some further issues that EnviFlux may be used to study. Appendices A, B, and C describe the formulation, use, and calibration of the spectral-based scheme used for the background error covariance matrix, which comprises a significant part of the system. Appendix D describes the way the software is structured, including the core code (written in C++), and visualisation/post-processing tools (written in python). EnviFlux also has a user guide, which complements this paper with some algorithmic details and instructions to run the software. The user guide is available in the GitHub repository (Bannister, 2026), and the code will be made available later.

2 Description of the system and the forward problem

EnviFlux has many components that work together to estimate the global surface fluxes. This section is a scientific description of the basic components that comprise the forward part of the system. Some finer details are documented in the user guide.

2.1 The continuous equations of motion

The continuous equation of motion for the tracer, χ, in 3D is nominally

$$\frac{\partial \chi(t)}{\partial t} + \boldsymbol{u}(t) \cdot \nabla \chi(t) = \mathbf{S}\rho(t) + \kappa_{\mathrm{h}} \nabla_{\mathrm{h}}^2 \chi(t) + \kappa_{\mathrm{v}} \frac{\partial^2 \chi(t)}{\partial z^2}, \tag{1}$$

where $\boldsymbol{u}$ is the 3D wind vector ($\boldsymbol{u} = \begin{pmatrix} u & v & w \end{pmatrix}$), ρ is the 2D surface flux field, the operator $\mathbf{S}\rho$ constructs a 3D field of zero apart from the surface where it assigns the value $\rho/(\Delta z_0 d_0)$ (surface layer thickness Δz_0, surface air density $d_0 = 1.225\,\mathrm{kgm}^{-3}$), κ_{h} and κ_{v} are the horizontal and vertical diffusion coefficients, ∇ is the 3D gradient operator, and ∇_{h}^2 and $\partial^2/\partial z^2$ are the horizontal and vertical Laplacian operators. In practice, Eq. (1) is solved on a discrete grid in space and time (see below). In EnviFlux, χ has units of ppb, and ρ has units of $\mu\mathrm{gm}^{-2}\mathrm{s}^{-1}$.

https://doi.org/10.5194/egusphere-2025-6352
Preprint. Discussion started: 10 March 2026

2.2 The state vector, the spatial grid, and time-stepping

The core component of EnviFlux is the state vector, $\mathbf{x}$, which comprises the initial and boundary conditions needed to make predictions of the atmospheric tracer mixing ratio, $\boldsymbol{\chi}(t)$. The state vector is written

$$\mathbf{x} = \begin{pmatrix} \boldsymbol{\chi}(0) \\ \hline \boldsymbol{\rho}(0) \\ \boldsymbol{\rho}(\tau_\rho) \\ \vdots \\ \boldsymbol{\rho}(T\tau_\rho) \end{pmatrix}, \tag{2}$$

where $\boldsymbol{\chi}(0)$ is the initial 3D tracer field, and $\boldsymbol{\rho}(n\tau_\rho)$ is the surface flux field at a set of equally spaced time-steps $n = 0, 1, \ldots, T$. Bold symbols indicate the variables are part of the state vector. In this paper sometimes only the $\boldsymbol{\chi}(0)$ part of $\mathbf{x}$ is referred to and other times only the $\boldsymbol{\rho}(0), \ldots, \boldsymbol{\rho}(T\tau_\rho)$ part. The notation $\{\mathbf{x}\}_\chi$ and $\{\mathbf{x}\}_\rho$ shall refer to these parts respectively.

The spatial grid is shown in Fig. 1, which has n_x longitudes, n_y latitudes, and n_z vertical levels. The time-stepping is done in three stages, namely (i) the semi-Lagrangian (SL) advection stage, (ii) the diffusion stage, and (iii) the flux stage, which are described below. EnviFlux uses four kinds of time step, which are as follows (see Fig. 2).

- The *minor time step*, δt, is the interval used to divide up the back-trajectory for the solver needed for the SL advection scheme.
- The *diffusion time step*, τ_κ, is the time step used to solve the diffusion part of Eq. (1).
- The *major time step*, Δt, is the interval between the files specifying $\boldsymbol{u}$. It is also used as the length of time of each back-trajectory, which is divided into $\Delta t/\delta t$ sub intervals.
- The *flux time step*, τ_ρ (mentioned above), is the time interval between flux fields.

The values of these steps are restricted such that $\Delta t/\delta t$, $\Delta t/\tau_\kappa$, and $\tau_\rho/\Delta t$ are positive integers. The three stages of the model's time-stepping (over a major time step, Δt) are as follows.

1. The first stage solves the advection part of Eq. (1) with the SL method. Each χ point on the grid is taken as a "starting point" in a back trajectory calculation from time t back to $t - \Delta t$. This time is divided into smaller steps of size δt where the backward path for each is calculated using fourth-order Runge-Kutta (Press et al., 2007). This leads to an "end point" at $t - \Delta t$ for each trajectory. The "start" and "end" are in inverted commas as a reminder that these are meant in a backward time sense. The value of χ at the "starting point" at time t after this first stage is replaced by the value of χ at the "end point" at $t - \Delta t$. This involves spatial interpolation. EnviFlux allows tri-linear or tri-cubic interpolation, with the latter recommended to reduce loss of conservation.
2. The second stage solves the diffusion part of Eq. (1). Practically, the advected field from stage 1 is copied back to $t - \Delta t$ and a pure diffusion equation (Eq. (1) without the advection and flux terms) is integrated using standard finite-differences with steps of size τ_κ to time t. For the experiments shown in this paper, no explicit diffusion is applied.

https://doi.org/10.5194/egusphere-2025-6352
Preprint. Discussion started: 10 March 2026

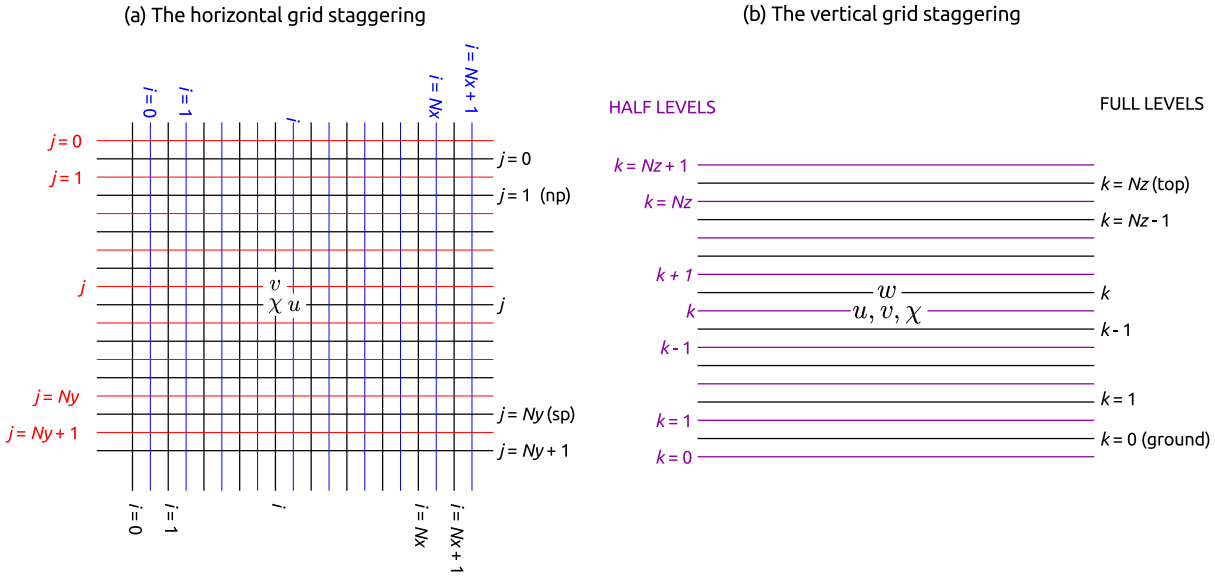

Figure 1. The horizontal (a) and vertical (b) model grids used for EnviFlux. In the horizontal, the tracer (χ), flux (ρ), and vertical wind (w) are stored at points where the black lines cross and indexed with the black i and j. The zonal wind (u) is stored at intermediate longitudes indexed with the blue i, and at the same latitudes as χ. The meridional wind (v) is stored at the same longitudes as χ, and intermediate latitudes indexed with the red j. The north (np) and south (sp) poles lie on black latitudes. This is the Arakawa "C" grid. In EnviFlux the longitudes are equally spaced, but the latitudes are Gaussian latitudes, which are not equally spaced (this is to allow accurate application of a spherical transform used to model the $\mathbf{B}$-matrix – see Sect. 3.3). In the vertical, χ, u, and v are stored on "half levels" indexed with the purple k, and w is stored on "full levels" indexed with the black k. This is the Charney-Phillips staggering.

3. The third stage introduces the surface fluxes to the model's layer closest to the surface with an increment of $\boldsymbol{\rho} \times \Delta t/(d_0 \Delta z_0)$, where d_0 and Δz_0 are defined above. This form assumes that the fluxes add tracer to or remove tracer from the air uniformly within the surface grid layer at each horizontal position. The particular flux field time in the state vector (2) used in this step is simply $\mathrm{int}(t/\tau_\rho)$, where the $\mathrm{int}(\bullet)$ function rounds down to the nearest integer. In other words the $\boldsymbol{\rho}(n\tau_\rho)$ is the flux field valid between times $n\tau_\rho \le t < (n+1)\tau_\rho$.

The output of the third stage approximates the solution of Eq. (1) at time t. The approximations made in these steps are assumed to be adequate for this simplified system. At the moment, EnviFlux does not include (sub-grid) turbulent or convective transport processes.

For the rest of this paper, we shall represent these three steps with the linear propagator $\boldsymbol{\chi}(k\Delta t) = \mathbf{M}^{\{\mathbf{x}\}_\rho}_{k-1\to k}\boldsymbol{\chi}([k-1]\Delta t)$, where the $\{\mathbf{x}\}_\rho$ superscript indicates that the propagator is dependent on the surface flux part of the state vector, Eq. (2), which obviously influences the model trajectory. The surface flux does not get updated, which is why it is not part of the main argument. There are three caveats about the meaning of this propagator. The first is that when $k-1=0$ the argument of $\mathbf{M}^{\{\mathbf{x}\}_\rho}_{k-1\to k}$, i.e. $\boldsymbol{\chi}(0)$, must be identical to the tracer component of the state vector, i.e. $\{\mathbf{x}\}_\chi$. The propagator definition may

https://doi.org/10.5194/egusphere-2025-6352
Preprint. Discussion started: 10 March 2026

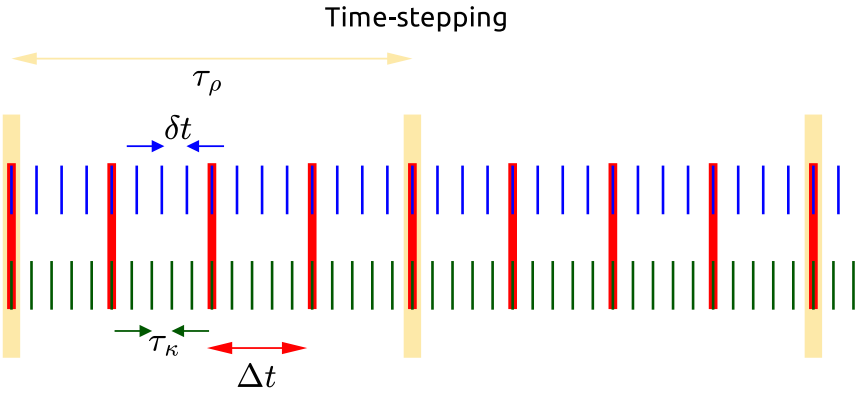

Figure 2. Timeline showing the time-stepping schemes used by EnviFlux, showing the four time intervals used. The back trajectories used for the semi-Lagrangian advection are of time length Δt, which are comprised of minor time-steps, δt. Δt is also the time interval of the wind files. Explicit diffusion effects are introduced with a timestep τ_κ, and the flux fields have a time interval of τ_ρ.

therefore be refined:

$$\boldsymbol{\chi}(k\Delta t) = \begin{cases} \mathbf{M}^{\{\mathbf{x}\}_\rho}_{k-1\to k}\boldsymbol{\chi}([k-1]\Delta t) & k-1>0 \\ \mathbf{M}^{\{\mathbf{x}\}_\rho}_{k-1\to k}\{\mathbf{x}\}_\chi & k-1=0. \end{cases} \tag{3}$$

The second and third caveats are covered in the next section.

2.3 The adjoint step

The second caveat concerns the adjoint operator, i.e. $\hat{\boldsymbol{\chi}}([k-1]\Delta t) := \left(\mathbf{M}^{\{\hat{\mathbf{x}}\}_\rho}_{k-1\to k}\right)^{\mathsf{T}}\hat{\boldsymbol{\chi}}(k\Delta t)$. The action of the adjoint propagates gradient[1] information (indicated with the hat) from $\hat{\boldsymbol{\chi}}(k\Delta t)$ backwards in time to $\hat{\boldsymbol{\chi}}([k-1]\Delta t)$. Additionally, this operator must incrementally update the gradient state $\{\hat{\mathbf{x}}\}_\rho$. The third caveat concerns the action of the adjoint at the earliest time. While when $t-\Delta t>0$, the output of the adjoint operator is the tracer gradient, $\hat{\boldsymbol{\chi}}([k-1]\Delta t)$ (and update of $\{\hat{\mathbf{x}}\}_\rho$), as indicated above, in the special case when $k-1=0$, i.e. $\left(\mathbf{M}^{\{\hat{\mathbf{x}}\}_\rho}_{0\to 1}\right)^{\mathsf{T}}$, the output will be defined as the gradient of the whole state vector. In summary:

$$\left(\mathbf{M}^{\{\hat{\mathbf{x}}\}_\rho}_{k-1\to k}\right)^{\mathsf{T}}\hat{\boldsymbol{\chi}}(k\Delta t) := \begin{cases} \hat{\boldsymbol{\chi}}([k-1]\Delta t) & k>1 \\ \begin{pmatrix} \hat{\boldsymbol{\chi}}(0) \\ \hat{\boldsymbol{\rho}}(0) \\ \hat{\boldsymbol{\rho}}(\tau_\rho) \\ \vdots \\ \hat{\boldsymbol{\rho}}(T\tau_\rho) \end{pmatrix} & k=1, \end{cases} \tag{4}$$

[1] Gradient of the observation term of the cost function, see Eqs. (5) and (6).

https://doi.org/10.5194/egusphere-2025-6352
Preprint. Discussion started: 10 March 2026

where the $\hat{\boldsymbol{\rho}}$ are the accumulations of increments held in the $\{\hat{\mathbf{x}}\}_\rho$ superscript during the course of the adjoint operations (as mentioned in caveat 2). This definition is for notational convenience when computing the gradient of the cost function (see Sect. 3.1).

3 Description of the inverse problem

This section is a description of how the surface fluxes are inferred from observations.

3.1 The cost function

EnviFlux uses an incremental formulation of the cost function that is minimised during the 4D-Var. In this formulation, $\mathbf{x} = \mathbf{x}^\mathrm{b} + \delta\mathbf{x}$, where $\mathbf{x}^\mathrm{b}$ is the background field (a-priori), and $\delta\mathbf{x}$ is the increment, found by minimising the 4D-Var cost function. Instead of varying $\delta\mathbf{x}$ directly, a control variable, $\delta\mathbf{v}$ is varied, where $\delta\mathbf{x}$ and $\delta\mathbf{v}$ are related via $\delta\mathbf{x} = \mathbf{B}^{1/2}\delta\mathbf{v}$, where $\mathbf{B}$ is the background error covariance matrix (Sect. 3.3). This change of variable removes the $\mathbf{B}$-matrix in explicit form from the cost function, and helps improve the conditioning (see e.g. Bannister (2008b) or Sect. 3.1 of Bannister (2026)). In terms of $\delta\mathbf{v}$ the cost function is

$$J_{\delta\mathbf{v}}(\delta\mathbf{v}) = \frac{1}{2}\delta\mathbf{v}^\intercal\delta\mathbf{v} + \frac{1}{2}\sum_{k=0}^{N_T}\left(\mathbf{y}_k - \mathbf{H}_k\mathbf{M}_{0\to k}^{\left\{\mathbf{x}^\mathrm{b}+\mathbf{B}^{1/2}\delta\mathbf{v}\right\}_\rho}\left[\boldsymbol{\chi}^\mathrm{b}(0) + \left\{\mathbf{B}^{1/2}\delta\mathbf{v}\right\}_\chi\right]\right)^\intercal \mathbf{R}_k^{-1}(\bullet), \tag{5}$$

where the notation $\{\mathbf{x}\}_\chi$ and $\{\mathbf{x}\}_\rho$ is explained in Sect. 2.2, N_T is the number of major time-steps in the problem, $\mathbf{y}_k$ is the set of observations made at time-step k, $\mathbf{H}_k$ is the observation operator, $\mathbf{R}_k$ is the observation error covariance matrix, and $\boldsymbol{\chi}^\mathrm{b}(0) = \left\{\mathbf{x}^\mathrm{b}\right\}_\chi$ is the background tracer at $t = 0$. The "$\mathbf{a}^\intercal\mathbf{A}^{-1}\bullet$" notation is shorthand for "$\mathbf{a}^\intercal\mathbf{A}^{-1}\mathbf{a}$", for brevity. Even though the notation in Eq. (5) implies that observations are at major time-steps only, EnviFlux does allow observations to be made at intermediate times, which are treated with linear interpolation (for details see Sect. 3.2.1 of Bannister (2026)).

The gradient of the cost function is

$$\nabla_{\delta\mathbf{v}}J(\delta\mathbf{v}) = \delta\mathbf{v} - \mathbf{B}^{\intercal/2}\sum_{k=0}^{N_T}\left(\mathbf{M}_{0\to k}^{\left\{\mathbf{x}^\mathrm{b}+\mathbf{B}^{1/2}\delta\mathbf{v}\right\}_\rho}\right)^\intercal \mathbf{R}_k^{-1}\left(\mathbf{y}_k - \mathbf{H}_k\mathbf{M}_{0\to k}^{\left\{\mathbf{x}^\mathrm{b}+\mathbf{B}^{1/2}\delta\mathbf{v}\right\}_\rho}\left[\boldsymbol{\chi}^\mathrm{b}(0) + \left\{\mathbf{B}^{1/2}\delta\mathbf{v}\right\}_\chi\right]\right), \tag{6}$$

where $\mathbf{B}^{\intercal/2} = \left(\mathbf{B}^{1/2}\right)^\intercal$, which is fed to a conjugate gradient-based descent algorithm (Golub and Van Loan, 1996; Lewis et al., 2006) to iteratively minimise the cost function. A version of the gradient calculation that is more efficient to compute than Eq. (6) is used by EnviFlux (see Sect. 3.2.2 of Bannister (2026)).

https://doi.org/10.5194/egusphere-2025-6352
Preprint. Discussion started: 10 March 2026

The block partitioning of $\delta\mathbf{v}$ is similar to that of $\mathbf{x}$ in Eq. (2) in the sense that the first part concerns the initial conditions and the remainder concerns the surface fluxes:

$$\delta\mathbf{v} = \begin{pmatrix} \text{initial conditions} \\ \hline \\ \text{surface fluxes} \\ \\ \end{pmatrix}. \tag{7}$$

The size of each block in $\delta\mathbf{v}$ is the same as in $\mathbf{x}$, but the elements have different meanings. The elements represent weights of different spectral components, and vertical or temporal modes. This is discussed further in Sect. (3.3).

3.2 Observations and observation operators

EnviFlux allows three types of observation to be assimilated, namely in situ tracer observations, total column amount (TCA) observations, and direct flux observations. Observations can be at any geographical location, and tracer observations can additionally be made at any height above the surface within the domain. The model's version of the observations, $\mathbf{H}_k\boldsymbol{\chi}(k\Delta t)$, are found by linear interpolation in space and time. The TCA observations are found from a discretisation of the vertical integral $\int \chi(z)d_z dz$, where z is height above the surface, d_z is the air density, and $\chi(z)$ is the tracer field interpolated to the geographical location and time of each observation.

Currently in EnviFlux, observation errors are assumed uncorrelated. The observation error standard deviations, σ^{o}, can be set arbitrarily for each observation, and the diagonal elements of the $\mathbf{R}$-matrix is made up of values $\sigma^{\mathrm{o}2}$. EnviFlux uses these observation operators in the assimilation, and the same operators are used to make synthetic observations as part of the twin experiment method.

3.3 The background error covariance matrix

The background error covariance matrix, or $\mathbf{B}$ for short, is a fundamental component of a Gaussian-based Bayesian problem, such as that described by Eq. (5). As in most assimilation systems, the probability density function of background errors is assumed to be Gaussian, where the mean is $\mathbf{x}^{\mathrm{b}}$ and the error covariance is $\mathbf{B}$. The $\mathbf{B}$-matrix specifies, statistically, how large background errors are and how background errors are correlated, e.g. Bannister (2008a). The background term of the unprecondioned cost function – when written in terms of $\delta\mathbf{x}$, see Eq. (6) of Bannister (2026) – is proportional to minus the logarithm of this PDF.

In the preconditioned cost function, Eq. (5), the new variable, $\delta\mathbf{v}$, is chosen to have unit background error covariances, which means that the background errors in this $\delta\mathbf{v}$-representation are uncorrelated and have unit variance. The $\mathbf{B}$-matrix appears in this preconditioned system via a square-root in the variable transform $\mathbf{B}^{1/2}$, i.e. $\delta\mathbf{x} = \mathbf{B}^{1/2}\delta\mathbf{v}$ (for more details about this kind of variable transform, see e.g. Bannister (2008b) or Bannister (2020)). $\mathbf{B}^{1/2}$ is a large matrix, and so instead of storing it explicitly, it is formulated with a set of component operators, called a background error covariance model. In practice these are

https://doi.org/10.5194/egusphere-2025-6352
Preprint. Discussion started: 10 March 2026

compactly encoded as subroutines. In EnviFlux it has the following form:

$$\mathbf{B}^{1/2} = \left(\begin{array}{c|c} \boldsymbol{\Sigma}^{\mathrm{b}}_{\chi}\mathbf{F}_{\mathrm{v}\chi}\boldsymbol{\Lambda}^{1/2}_{\mathrm{v}\chi}\mathbf{F}^{\mathsf{T}}_{\mathrm{v}\chi}\mathbf{R}_{\mathrm{h}}\mathbf{S}_{\mathrm{h}}\boldsymbol{\Lambda}^{1/2}_{\mathrm{h}\chi} & \mathbf{0} \\ \hline \mathbf{0} & \boldsymbol{\Sigma}^{\mathrm{b}}_{\rho}\mathbf{F}_{\mathrm{t}\rho}\boldsymbol{\Lambda}^{1/2}_{\mathrm{t}\rho}\mathbf{F}^{\mathsf{T}}_{\mathrm{t}\rho}\mathbf{R}_{\mathrm{h}}\mathbf{S}_{\mathrm{h}}\boldsymbol{\Lambda}^{1/2}_{\mathrm{h}\rho} \end{array}\right), \tag{8}$$

which acts on $\delta\mathbf{v}$ of the form of Eq. (7). The top-left block operates on the initial condition part of $\delta\mathbf{v}$ and the bottom-right block operates on the flux part of $\delta\mathbf{v}$, and there is no coupling between them in this choice of model. Alternative $\mathbf{B}$-matrix models may be coded instead, but the parts of this $\mathbf{B}^{1/2}$, associated with the initial conditions and fluxes, are now explained in turn.

3.3.1 The part of $\mathbf{B}^{1/2}$ associated with the initial conditions

The first part of $\mathbf{B}^{1/2}$ is associated with the initial conditions, $\boldsymbol{\chi}(0)$ (upper left in (8)).

1. In the order of operation, the first stage ($\mathbf{S}_{\mathrm{h}}\boldsymbol{\Lambda}^{1/2}_{\mathrm{h}\chi}$) models horizontal correlations of $\boldsymbol{\chi}(0)$. Suppose that horizontal correlations are represented by the matrix $\mathbf{C}_{\mathrm{h}\chi}$. This can be written in its eigenvalue decomposition $\mathbf{C}_{\mathrm{h}\chi} = \mathbf{S}_{\mathrm{h}}\boldsymbol{\Lambda}_{\mathrm{h}\chi}\mathbf{S}^{\mathsf{T}}_{\mathrm{h}}$, where $\boldsymbol{\Lambda}_{\mathrm{h}\chi}$ is the (diagonal) matrix of eigenvalues, and $\mathbf{S}_{\mathrm{h}}$ is the matrix of eigenvectors. This form justifies this particular square-root, $\mathbf{S}_{\mathrm{h}}\boldsymbol{\Lambda}^{1/2}_{\mathrm{h}\chi}$ (so that the square-root multiplied by its transpose gives $\mathbf{C}_{\mathrm{h}\chi}$). Here, $\mathbf{S}_{\mathrm{h}}$ is chosen to be a spherical spectral transform (transforming from a spectral space representation of the control vector to a grid space representation), so the eigenvectors have the assumed form of spherical harmonics. The spectral representation is a grid of wavenumbers ℓ (the "degree" wavenumber), m (the "order" wavenumber) (see Appendix A), and vertical level. The form of the transform is symbolic only, as practically the horizontal transform is applied separately for each vertical level (as a Kronecker product). The diagonals of $\boldsymbol{\Lambda}_{\mathrm{h}\chi}$ are prescribed functions of ℓ, which goes from 0 to the maximum value L (where $n_x = 2L+1$ and $n_y = L+1$) and we use the same function for each vertical level. The shape of $\boldsymbol{\Lambda}_{\mathrm{h}\chi}$ sets the horizontal lengthscale for initial tracer background errors. $\mathbf{S}_{\mathrm{h}}$ uses the *SHTools* software (Wieczorek et al., 2018). A tutorial on this horizontal transform is given in Appendix A, how it is applied in Appendix B1, and how $\boldsymbol{\Lambda}_{\mathrm{h}\chi}$ is found in Appendix C1. The natural output grid for $\mathbf{S}_{\mathrm{h}}$ is a Gaussian grid, and *SHTools* uses co-latitudes. EnviFlux uses the same Gaussian grid and the reconfiguration $\mathbf{R}_{\mathrm{h}}$ operator here just transforms from co-latitudes to geographical latitudes.

2. The next stage ($\mathbf{F}_{\mathrm{v}\chi}\boldsymbol{\Lambda}^{1/2}_{\mathrm{v}\chi}\mathbf{F}^{\mathsf{T}}_{\mathrm{v}\chi}$), models vertical correlations. The eigenvector and eigenvalue matrices ($\mathbf{F}_{\mathrm{v}\chi}$ and $\boldsymbol{\Lambda}_{\mathrm{v}\chi}$ respectively, each $n_z \times n_z$ matrices) are derived from the proposed vertical correlation matrix shown in Fig. 3. Again, this transform is symbolic only, as practically the vertical matrices are applied separately for each horizontal position (as a Kronecker product). Practical notes are given in Appendix B2, how $\mathbf{F}_{\mathrm{v}\chi}$ and $\boldsymbol{\Lambda}_{\mathrm{v}\chi}$ are found is described in Appendix C2.

https://doi.org/10.5194/egusphere-2025-6352
Preprint. Discussion started: 10 March 2026

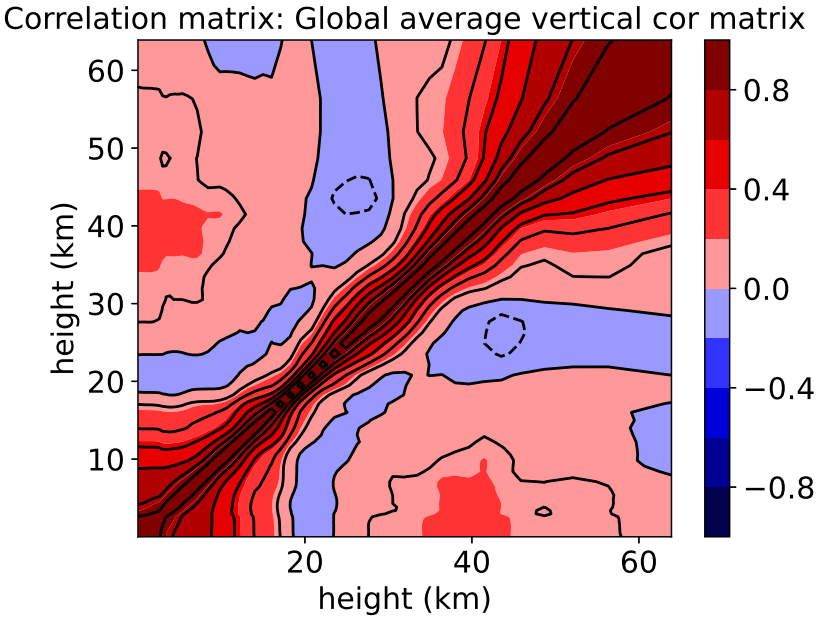

Figure 3. The vertical error correlation matrix for $\boldsymbol{\chi}(0)$, which is used to find the eigenvectors, $\mathbf{F}_{\mathrm{v}\chi}$, and eigenvalues, $\boldsymbol{\Lambda}_{\mathrm{v}\chi}$. This matrix is computed according to the procedure outlined in Appendix C2.

3. The last matrix, $\boldsymbol{\Sigma}^{\mathrm{b}}_{\chi}$, is a diagonal matrix and specifies how background error standard deviations of the initial tracer depend on position in space. This is discussed in Sect. 3.3.3.

3.3.2 The part of $\mathbf{B}^{1/2}$ associated with the fluxes

The second part of $\mathbf{B}^{1/2}$ is that associated with the surface fluxes, $\boldsymbol{\rho}$ (bottom right in Eq. (8)).

4. The first stage is $\mathbf{S}_{\mathrm{h}}\boldsymbol{\Lambda}^{1/2}_{\mathrm{h}\rho}$. This is similar to point 1 above and again the form is symbolic only, as practically the transform is applied separately to each of the $T+1$ flux times. The diagonals of $\boldsymbol{\Lambda}_{\mathrm{h}\rho}$ form a prescribed function of ℓ. The shape of $\boldsymbol{\Lambda}_{\mathrm{h}\rho}$ sets the horizontal lengthscale for flux background errors. See Appendices A, B1, and C1. The $\mathbf{R}_{\mathrm{h}}$ operator is the same as in point 1 above.

5. The next stage is $\mathbf{F}_{\mathrm{t}\rho}\boldsymbol{\Lambda}^{1/2}_{\mathrm{t}\rho}\mathbf{F}^{\mathsf{T}}_{\mathrm{t}\rho}$, which models temporal correlations for $\boldsymbol{\rho}$. The temporal eigenvectors, $\mathbf{F}_{\mathrm{t}\rho}$, and eigenvalues, $\boldsymbol{\Lambda}_{\mathrm{t}\rho}$, are derived from a prescribed $(T+1)\times(T+1)$ temporal correlation matrix with a specified correlation timescale. See Appendices B3 and C3.

https://doi.org/10.5194/egusphere-2025-6352
Preprint. Discussion started: 10 March 2026

6. The last matrix, $\mathbf{\Sigma}^{\mathrm{b}}_{\rho}$ (see Sect. 3.3.3), is a diagonal matrix and specifies how background error standard deviations in $\boldsymbol{\rho}(0), \ldots, \boldsymbol{\rho}(T\tau_\rho)$ depend on position in space. $\mathbf{\Sigma}^{\mathrm{b}}_{\rho}$ has the following $(T+1)\times(T+1)$ block form:

$$\mathbf{\Sigma}^{\mathrm{b}}_{\rho} = \begin{pmatrix} \mathbf{\Sigma}^{\mathrm{b}}_{\rho(0)} & & \\ & \ddots & \\ & & \mathbf{\Sigma}^{\mathrm{b}}_{\rho(T\tau_\rho)} \end{pmatrix}. \tag{9}$$

As the $\boldsymbol{\chi}$ and $\boldsymbol{\rho}$ parts in $\mathbf{B}^{1/2}$ are separate, this assumes that background errors between these are uncorrelated. Including such coupling is beyond the scope of this work.

3.3.3 The background error standard deviations, $\mathbf{\Sigma}^{\mathrm{b}}_{\boldsymbol{\chi}}$ and $\mathbf{\Sigma}^{\mathrm{b}}_{\boldsymbol{\rho}}$

The background error standard deviation fields (diagonals of $\mathbf{\Sigma}^{\mathrm{b}}_{\chi}$ and $\mathbf{\Sigma}^{\mathrm{b}}_{\rho}$) influence how much information is provided by the background verses the observations. $\mathbf{\Sigma}^{\mathrm{b}}_{\chi}$ is a function of longitude, latitude, and height, and $\mathbf{\Sigma}^{\mathrm{b}}_{\rho}$ is a function of longitude, latitude, and time (in time intervals of τ_ρ). Where and when the background error standard deviation is larger, the assimilation has less confidence in the background and so gives more relative weight to the observations. The particular choices of $\mathbf{\Sigma}^{\mathrm{b}}_{\chi}$ and $\mathbf{\Sigma}^{\mathrm{b}}_{\rho}$ can be chosen arbitrarily.

4 A "weakly Bayesian" example for source/sink location detection

A first demonstration is to investigate how well EnviFlux can identify the locations (and "strengths") of a pair of localised flux features from observations only. The details of these experiments, including the background error covariance specifications and the observation details, are provided in the middle column of Table 1. Figure 4 shows the initial conditions and flux field used as the truth for this experiment. The pair of features comprises a source point of peak strength 0.004 $\mu\mathrm{g m^{-2} s^{-1}}$ and a sink point of peak strength 0.005 $\mu\mathrm{g m^{-2} s^{-1}}$. The source location reflects a real-world emission location of methane – see, e.g. Fig. 4 of Qu et al. (2021) – but the sink location is chosen for curiosity only, as in reality methane sinks are not localised in this way.

In these experiments, no a-priori information about the features' positions is provided. The a-priori (background) state for the initial conditions is a perturbed version of the truth found with $\mathbf{B}^{1/2}\delta\mathbf{v}$, where $\delta\mathbf{v}$ is a random vector in control space with elements drawn from $N(0,1)$. On the colour scale of Fig. 4(a), the perturbed field is barely distinguishable, so is not shown. The a-priori state for the flux field is a zero field at each source time-step over the 100 day experiment, meaning that the system has no a-priori information about the locations, making this an interesting and challenging test of the inverse problem (something that could happen in a real-world application if sources or sinks appear that are not accounted for in the a-priori).

Two kinds of observations are separately assimilated, namely (i) total column amount (TCA) observations following an orbital track (see Table 1 for the details), and (ii) surface in situ (SIS) observations at the same geographical positions. Even though this reflects a realistic observational situation for the TCA observations (such as those made from GOSAT (Yokota et al., 2009) allowing for screening), it is not for SIS observations, but we study the SIS observations along the orbital track so

https://doi.org/10.5194/egusphere-2025-6352
Preprint. Discussion started: 10 March 2026

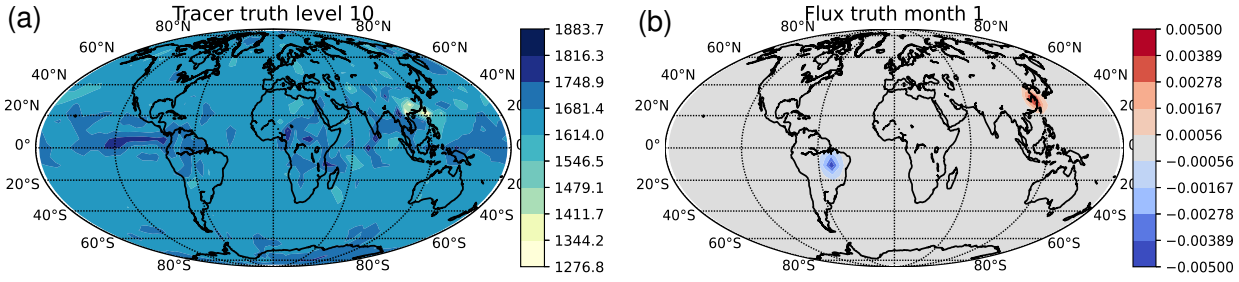

Figure 4. The true state chosen for the source/sink location detection experiments. Panel (a) is for $\chi^{\mathrm{t}}(0)$ at level 10 (850m above the ground, units ppb) and panel (b) is for $\rho^{\mathrm{t}}(0)$ (corresponding to the first 30 days, units $\mu\mathrm{g m}^{-2}\mathrm{s}^{-1}$). In (b), red is a source and blue is a sink.

the impact of the two observation types can be directly compared. This is a similar design strategy to that used by Basu et al. (2018). Here, each is taken as a point location in the horizontal, even though in reality the remotely-sensed observations can have a footprint of 10s of km (Yokota et al., 2009). Further, there is no need to account for representativess error (Hodyss and Nichols, 2015) here as the observations have been prepared with random error only.

4.1 Location experiments: "perfectly specified" assimilation results

The posterior (analysis) states that follow from a run of EnviFlux with near perfect specifications (meaning the $\mathbf{B}$-matrix is a near perfect reflection of the actual errors[2], the $\mathbf{R}$-matrix is a perfect reflection of observation errors, there is no model error, and there are no explicit biases) are shown in Fig. 5. In fact this Fig. shows the analysis increments: these allow the adjustments to the initial conditions to be shown clearly, and, given that the background flux field is zero, the flux increment field is the same as the flux analysis.

The increments to $\chi(0)$ are very similar between the two observation types TCA (a) and SIS (c) and there are no strong peaks/troughs in the increment fields at the two source/sink locations. If there were especially large positive increments at the source location and negative increments at the sink location, it would suggest that the system was treating the systematic lack/excess of tracer at these two respective locations (due to the $\rho^{\mathrm{b}} = 0$) was partly due to errors in $\chi^{\mathrm{b}}(0)$. In fact, the analysis increment patterns in $\chi(0)$ match those of the chosen background error field, $\chi^{\mathrm{b}}(0) - \chi^{\mathrm{t}}(0)$ (not shown), but of opposite sign, indicating that the assimilation is doing a good job at adjusting $\chi^{\mathrm{b}}(0)$ towards the truth, despite the large errors in ρ^{b}.

The flux analyses after assimilating the two observation types TCA (b) and SIS (d) show features in the correct places, c.f. Fig. 4(b). This shows the ability of inverse modelling systems like EnviFlux to identify locations of fluxes that are not known to the a-priori. There are, however, two major issues. One is the over-estimation of the geographical extent of the features and the other is the under-estimation of the peak fluxes (the analyses underestimate the peaks by more than a factor of 10). These findings are perhaps not surprising as an assimilation system naturally smooths-out information (see e.g. arguments about the resolution of inverse problems in Rodgers (2000)), and the assimilation is constraining the flux to be as close to zero as possible

[2]Apart from the flux field due to the nature of this experiment.

https://doi.org/10.5194/egusphere-2025-6352
Preprint. Discussion started: 10 March 2026

	Feature detection experiments	Quasi real-world experiments
Grid dimensions	$n_x = 33$, $n_y = 65$, $n_z = 56$	
Experiment length	100 days	
Minor time-step, δt	1 hour	
Major time-step, Δt	12 hours	
Source time-step, τ_ρ	30 days	
No. of 4D-Var iterations	25	
True state		
True state ($\chi(0)$)	Fig. 4(a)	Fig. 9(a)
True state (ρ)	Fig. 4(b)	Fig. 9(b)
	A-priori state	
A-priori mean ($\chi(0)$)	$\left\{\mathbf{x}^{\mathrm{t}} + \mathbf{B}^{1/2}\delta\mathbf{v}\right\}_\chi$	$\left\{\mathbf{x}^{\mathrm{t}} + \mathbf{B}^{1/2}\delta\mathbf{v}\right\}_\chi$
A-priori mean (ρ)	Zero	$\left\{\mathbf{x}^{\mathrm{t}} + \mathbf{B}^{1/2}\delta\mathbf{v}\right\}_\rho$
Background error covariance specifications		
$\mathbf{\Sigma}^{\mathrm{b}}_\chi$ (ppb)	4.2 (surface) to 3.5 (top, ~ 46 km)	
$\mathbf{\Sigma}^{\mathrm{b}}_\rho$ (μgm^{-2}s^{-1})	0.00002	0.002 land, 0.0002 sea
Horiz. corr. fn. shape ($\chi(0)$ and ρ)	Lorentzian	
Horiz. lengthscale ($\chi(0)$)	600 km	
Horiz. lengthscale (ρ)	400 km	
Vertical correlations ($\chi(0)$)	Fig. 3	
Temporal cor. fn. shape (ρ)	Lorentzian	
Timescale (ρ)	3 months	
Observations		
Horiz. locations	Locations below an orbit of period 98 mins, 98° inclination	
Type	Total column amount or surface in situ	
Frequency	Every 96 seconds	
Observation error variance specifications		
σ^{o}	35 mgm^{-2} (TCA), 4 ppb (SIS)	45 mgm^{-2} (TCA) 4 ppb (SIS)

Table 1. Specifications of the two sets of experiments that are done. The first set is for the feature detection experiments (Sect. 4, middle column) and the second set is for the flux adjustment experiments (Sect. 5, right column). The vector $\delta\mathbf{v}$ is defined as a vector of independent random numbers, each drawn from the Gaussian distribution $N(0,1)$. For each set of experiments, separate total column amount (TCA) and surface in situ (SIS) observations (Sect. 3.2) are assimilated. The geographical locations of the observations follow that of an orbiting satellite. The observation error standard deviations, σ^{o}, are determined by doing a run of the true state over the experimental period, and then taking $\sim 10\%$ of the standard deviation of the computed observations.

https://doi.org/10.5194/egusphere-2025-6352
Preprint. Discussion started: 10 March 2026

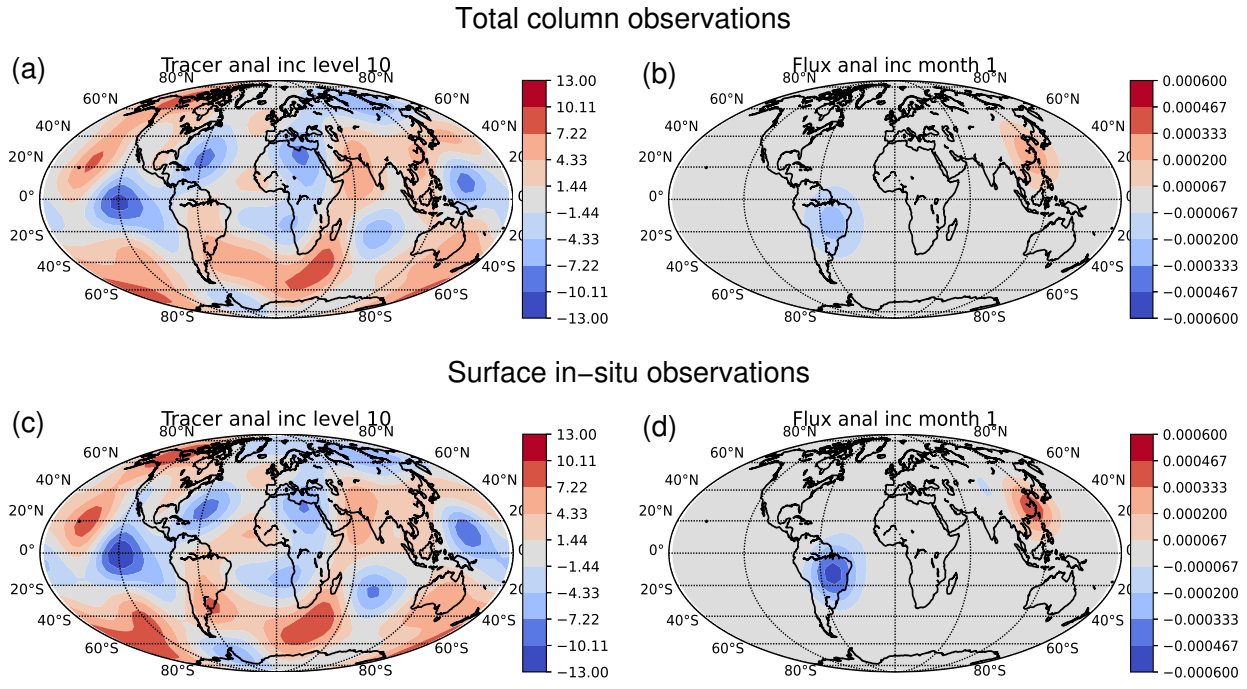

Figure 5. Analysis increments, $\delta\chi^{\mathrm{a}}(0)$ (units ppb) and $\delta\rho^{\mathrm{a}}(0)$ (units $\mu\mathrm{g m^{-2} s^{-1}}$), found by assimilating either TCA (top row) or SIS observations (bottom row) for the near perfect source/sink location detection experiments. Panels (a) and (c) are for $\delta\chi^{\mathrm{a}}(0)$ at level 10, and panels (b) and (d) are for $\delta\rho^{\mathrm{a}}(0)$. These plots should be compared to the true fields in Fig. 4. Red increments are positive and blue increments are negative. When comparing panels (b) and (d) to Fig. 4(b), note the different colour scales.

to match the prior. These two findings are linked. Arguably it is the area integrated source and sink fields that are important rather than the peak values, so if the analysed flux features are spatially smoothed, the peak values need to be reduced to keep the area integrated values stable. We found by trial-and-error that the relatively small value of $\mathbf{\Sigma}_{\rho}^{\mathrm{b}} = 0.00002\,\mu\mathrm{g m^{-2} s^{-1}}$ (see Table 1) keeps the integrated source and integrated sink values close to the true equivalents for the SIS observation system. Incidentally, significantly increasing the value of $\mathbf{\Sigma}_{\rho}^{\mathrm{b}}$ increases the analysed peak flux analysis values only marginally (not shown), supporting the argument that the assimilation constrains the integrated flux values more strongly than the specific peak values. This issue is studied more in the context of model error and observation bias in Sect. 4.3.

Interestingly, we find that TCA observations constrain the fluxes to a lesser degree than the SIS data can, despite the observing systems being set-up to have similar information coming from each (in the sense that the numbers of observations are the same and choosing σ^{o} values of the same percentage (10%) of the respective variabilities of the model's equivalents, see Table 1). This is an understandable result as a significant part of the TCA measurements originates away from the surface.

https://doi.org/10.5194/egusphere-2025-6352
Preprint. Discussion started: 10 March 2026

4.2 Location experiments: effect of model error and observation bias

We now study the effect of model error on the results. It is already known that transport uncertainties in the assimilation can influence the position and strength of sources, Yu et al. (2021), and we study this using the simple source/sink pair set-up. There are a number of ways of simulating model transport error, but it is simulated here by multiplying the vertical wind, w, in the assimilation by a number, η, close to unity (0.9 and 1.1), while the observations assimilated are still generated from samples from a run using the true winds (actually they are identical to those experiments in Sect. 4.1). Changing the vertical wind in this way modifies how well the tracer is circulated around the globe, and which levels (including jet levels) the tracer can easily reach. The reason for choosing this particular method is that it is simple to implement, and vertical transport is likely to be an important deficiency of real-world models. No attempt has been made here to account for the model error (e.g. by inflating σ^{o} as is done in other works, Lin and Gerbig (2005); Chevallier et al. (2010); Houweling et al. (2010)).

Figure 6 shows analysis increments of $\chi(0)$ (identical to the respective analysis fields in these experiments) with these two η values for the two observation types. The impact of these (rather modest) changes to vertical motion is greater in the assimilation of TCA than SIS observations. For the TCA observations, the ability of the system to identify the positions of the two flux features is almost completely destroyed for $\eta = 0.9$ (panel (a)). We refer to the property of an inferred flux field having a localised source and sink, such as in Fig. 5(b) as *coherent*; Fig. 6(a) is an example of *incoherence* in this field. This may be due to a weakening of the coupling between the above-surface tracer contributions to the TCA measurements, thus meaning that this part of the TCA is attributed to a whole range of diffuse locations around the globe (thinking in terms of back-trajectories from points along the vertical columns associated with these observations). The source location remains well identified in the $\eta = 1.1$ case (although shifted slightly south), but there is more than one sink location identified, although one is still in the right place (panel (b)). For the SIS observations, the ability of the assimilation to identify the two positions is more robust. The most noticeable effect is the shift of the centre of the source region eastwards by $\sim 5^{\circ}$ in panel (c), and the interpretation of some other regions as weak sources and sinks, such as Kazakhstan (an anomalous sink in panel (c)) and Greenland (an anomalous sink in (c) and source in (d)). The better results for SIS are expected, as these observations are more closely/directly influenced by the fluxes than the TCA observations are, and so are less affected by model error.

We also studied the effect of observation bias on the flux analysis. The results proved that the inferred positions of the flux features is robust against observation bias in the ranges studied (for biases up to just over half the value of σ^{o} for each observation type, analysis maps not shown). The flux amounts though are influenced by the bias, which is studied in the next section.

4.3 Location experiments: effect of model error on the peak source/sink locations and on flux values

A summary of the analysed fluxes found for the source/sink location experiments, while varying η is shown in Fig. 7. Panels (a) and (c) show how the global total and peak source/sink values vary with η (see the caption for definitions of the total and peak values). Panel (a) assimilates TCA and (c) assimilates SIS observations. For $\eta > 1$, there is a tendency for the global total and peak source amounts (red lines) to increase with η. For sources, increasing η generally distributes the sources to more distant

https://doi.org/10.5194/egusphere-2025-6352
Preprint. Discussion started: 10 March 2026

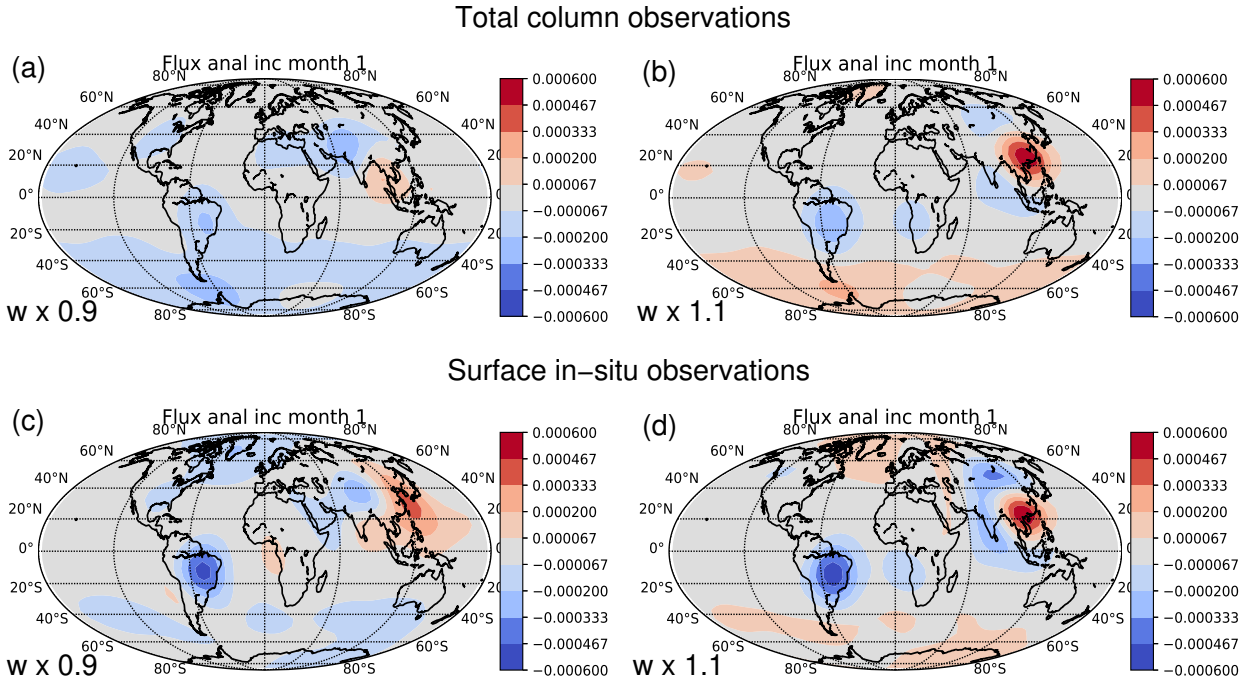

Figure 6. Analysis increments, $\delta\rho^{\mathrm{a}}(0)$ (units $\mu\mathrm{g m^{-2} s^{-1}}$), found by assimilating either TCA (top row) or SIS observations (bottom row) for the case when a proxy for model error is applied to the assimilation. Model error is simulated by multiplying the vertical wind, w, used in the assimilation by either $\eta = 0.9$ (panels (a) and (c)) or $\eta = 1.1$ (panels (b) and (d)). These plots should be compared to the true field in Fig. 4(b), but note the different colour scales (units $\mu\mathrm{g m^{-2} s^{-1}}$).

points downstream and so prevents the build-up of tracer at geographical locations close to the emissions. Hence larger fluxes are required to match the observations, which is found in the results for $\eta > 1$. A mirror argument may be made for the sinks (blue lines). It is harder to explain why the results show a strengthening of the total and peak sources and sinks as η gets smaller than particular values that depend on the experiment, e.g. $\eta < 0.8$ in (a). A possible explanation is that the DA is compensating for the increasing relative importance of numerical diffusion in the SL transport scheme as the winds get weaker, although this is just a supposition.

Further inspection of Fig. 7(a) and (c) reveals the following. The variations of the flux values are smaller for the SIS than for the TCA observations, which is not surprising as the SIS observations are less influenced by the global circulation. The relative variations of the global total flux values are much greater than for the peak flux values (total and peak values have different units – see the caption – which is why we refer to relative variations). The analysed global total values are mostly larger than the true global total values (compare solid lines with dashed lines) with the exception of $\eta \leq 1$ for the global total source (red solid line in (a)), but this will change with different values of $\mathbf{\Sigma}_{\rho}^{\mathrm{b}}$. The analysed peak values are always smaller than the true peak values (compare dotted lines with dot-dashed lines).

https://doi.org/10.5194/egusphere-2025-6352
Preprint. Discussion started: 10 March 2026

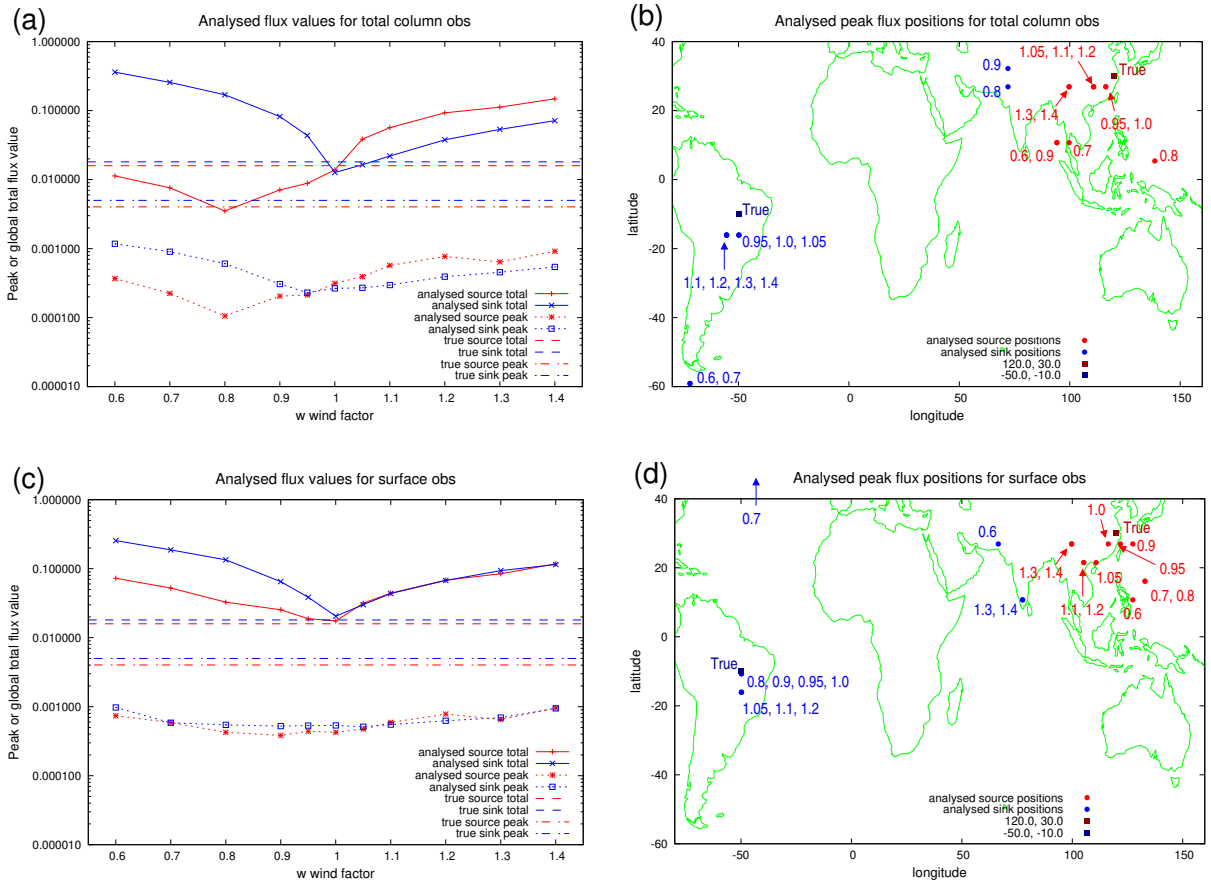

Figure 7. Summary of the effect of model error (via $w \to \eta w$) in the assimilation experiments for the detection of the source/sink locations. Panels (a) and (c) measure the analysed global total source, $\int_{\rho^{\mathrm{a}}(0)>0} dA\rho^{\mathrm{a}}(0)$ (red solid lines), total sink, $\left|\int_{\rho^{\mathrm{a}}(0)<0} dA\rho^{\mathrm{a}}(0)\right|$ (blue solid lines), peak source, $\max(\rho^{\mathrm{a}}(0))$ (red dotted lines), and peak sink, $|\min(\rho^{\mathrm{a}}(0))|$ (blue dotted lines). All flux analyses have some negative values, so $\min(\rho^{\mathrm{a}}(0))$ is always negative and so detects the strongest sink. The true source and sink values are indicated by the horizontal lines (dashed for true global total and dot-dashed for peak). The units are: global total values $\mathrm{Tg\,month^{-1}}$ and peak fluxes $\mu\mathrm{gm^{-2}s^{-1}}$. Panels (b) and (d) show the analysed positions of the peak source locations (red circles) and peak sink locations (blue circles). The numbers are values of η for each assimilation run. The true peak locations are shown as squares. The top plots are for the TCA and the bottom plots are for the SIS observations.

A further robust finding of these experiments is that the posterior errors in the fluxes are always smaller than the prior errors. This is not surprising because the prior flux is a zero field. The posterior errors in the initial conditions, however, are larger than the prior errors, except when $\eta = 0$ (not shown). This is an example of model error aliasing onto another component of the system, in this case the initial conditions.

https://doi.org/10.5194/egusphere-2025-6352
Preprint. Discussion started: 10 March 2026

Figure 7 (b) and (d) shows how the positions of the peak source (red dots) and sink (blue dots) change with η for the TCA (b) and SIS (d) observations. The true positions of the source and sink are shown as squares. Even though maximum and minimum flux positions are always found in $\rho^{\mathrm{a}}(0)$, the field patterns are not always coherent (e.g., compare Figs. 5(b) with 6(a)).

The inferred peak positions of the source form a "cloud" of locations inside SE Asia for both observation systems, with the $\eta = 0.95$ and 1.0 being closest for both observation systems. Even though $\rho^{\mathrm{a}}(0)$ for the $\eta = 0.9$ and TCA observations case loses its coherence (Fig. 6(a)), the $\eta = 0.95$ case (not shown) maintains a coherent a set of correctly positioned source and sink features. The positions inferred from the SIS observations are slightly more robust against deviations of η from 1.0.

As η deviates from unity, the inferred sink positions become more variable than the source positions. The $\rho^{\mathrm{a}}(0)$ sinks tend to be diagnosed at a more diverse range of locations, often on different continents to the true location. Often the analysed peak locations are close to the true locations, but these are usually just the strongest of many local peaks which the assimilation has constructed.

4.4 Location experiments: effect of observation bias on the source/sink locations and fluxes

Figure 8 shows how the global total, and the peak source and sink values vary with observation bias (there is no model error in these experiments). Panel (a) is for the TCA observations and (b) is for the SIS observations. Each different experiment assimilates similar observations discussed previously, but where an observation bias has been added. The amount of bias varies up to $\pm$ just over half of the value of σ^{o} for each observation type (see bottom row, middle column of Table 1). The peak source and sink values (red and blue dotted lines) are almost completely insensitive to the observation bias, but the total source and sink fluxes (solid lines) do show variation in the way expected (i.e. the total source fluxes increase with the values of the biases, and the total sink values decrease). This is a similar property of the system (mentioned but not shown in Sect. 4.3), that the analysed total flux values are sensitive to the choice of $\mathbf{\Sigma}_{\rho}^{\mathrm{b}}$, but the analysed peak values are not. Further, the locations and coherency of the source and sink features are unaffected by the range of biases studied (not shown).

5 A Bayesian example for a quasi-real-world situation

The localised flux experiments in Sect. 4 are an interesting way to study some of the factors that affect the ability of a flux inversion system to infer positions and strengths of individual features without the full guidance of a-priori information. In environmental science problems, the regions of strong sources and sinks are often multiple and more distributed, but the inversion has the benefit of more a-priori information. The a-priori information is a Gaussian PDF with a specified mean (the a-priori state, $\mathbf{x}^{\mathrm{b}}$) and covariance $\mathbf{B}$. We apply EnviFlux in a similar way to that in Sect. 4, but in a less idealised setting, and with an informative a-priori.

The set-up for these experiments is described in the right column of Table 1. The main differences with the previous experiments are a different true state, a more informative prior state, prior error standard deviations that are dependent on the surface type (values 10 times smaller over the sea than over land), and a $\sim 30\%$ larger σ^{o} for TCA observations. The latter difference is

https://doi.org/10.5194/egusphere-2025-6352
Preprint. Discussion started: 10 March 2026

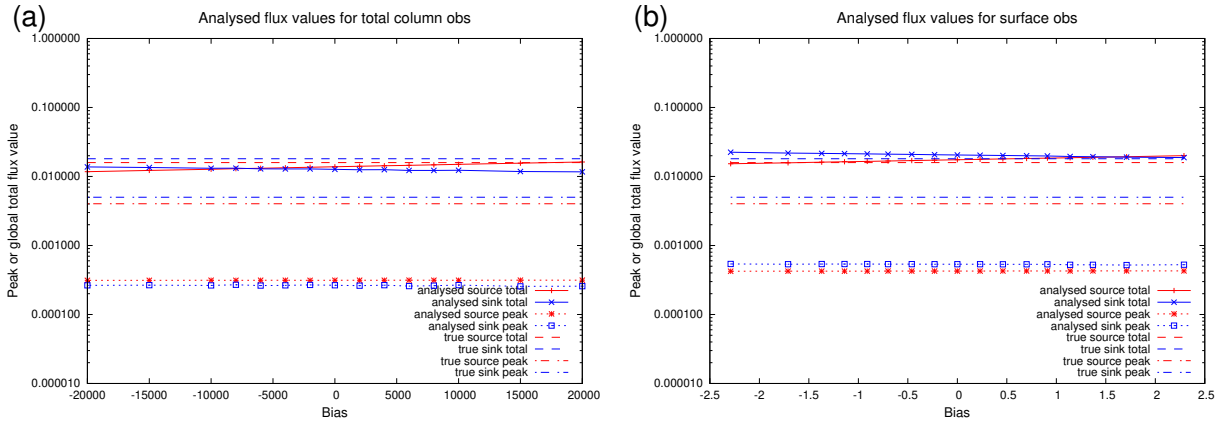

Figure 8. As Fig. 7(a) and (c) but for how the analysed global total, and the peak sources and sinks vary with observation bias. Panel (a) is for the TCA observations (observation units $\mathrm{Tg\,month^{-1}}$) and (b) is for the SIS observations (units $\mu\mathrm{gm^{-2}s^{-1}}$).

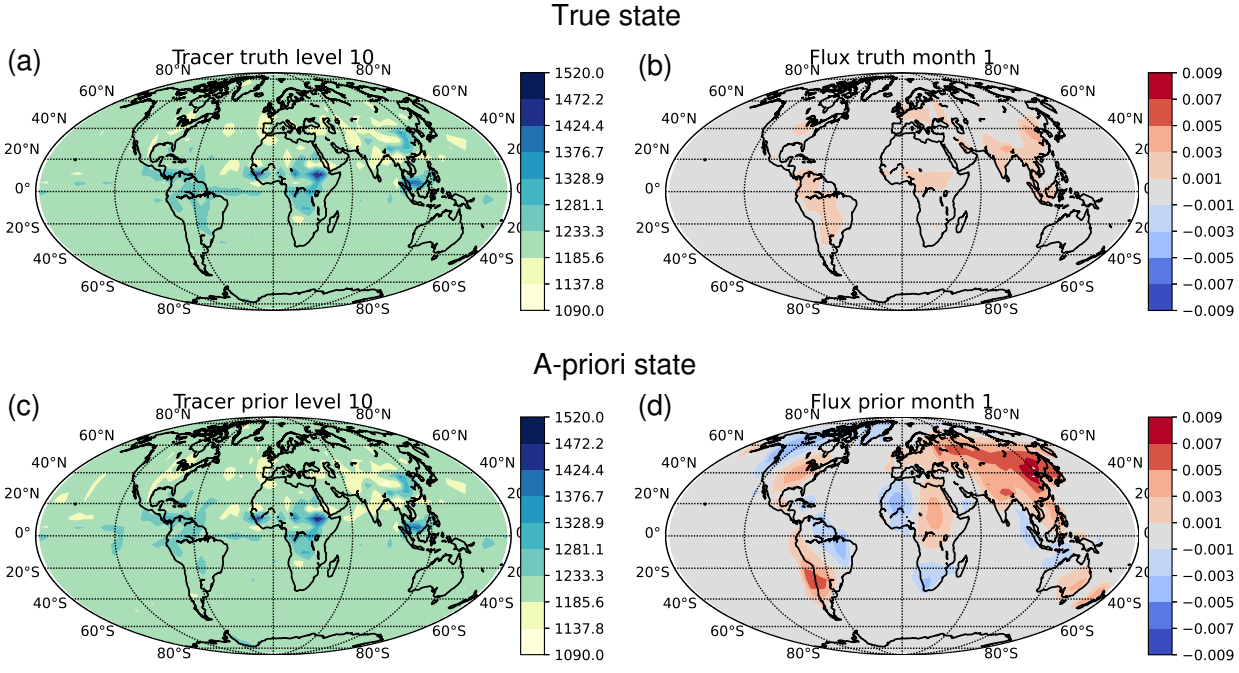

Figure 9. The true state (top row) and the a-priori state (bottom row) chosen for the quasi-real experiments. The left column is for $\chi(0)$ at level 10 (850m above the ground, units ppb) and the right column is for $\rho(0)$ (corresponding to the first 30 days, units $\mu\mathrm{gm^{-2}s^{-1}}$). In (b) and (d), red is a source and blue is a sink.

made because in these experiments, the variability in the TCA observations is $\sim 30\%$ larger than for the previous experiments; the SIS observations have around the same variability as the previous experiments, so σ^{o} for SIS observations is kept the same.

https://doi.org/10.5194/egusphere-2025-6352
Preprint. Discussion started: 10 March 2026

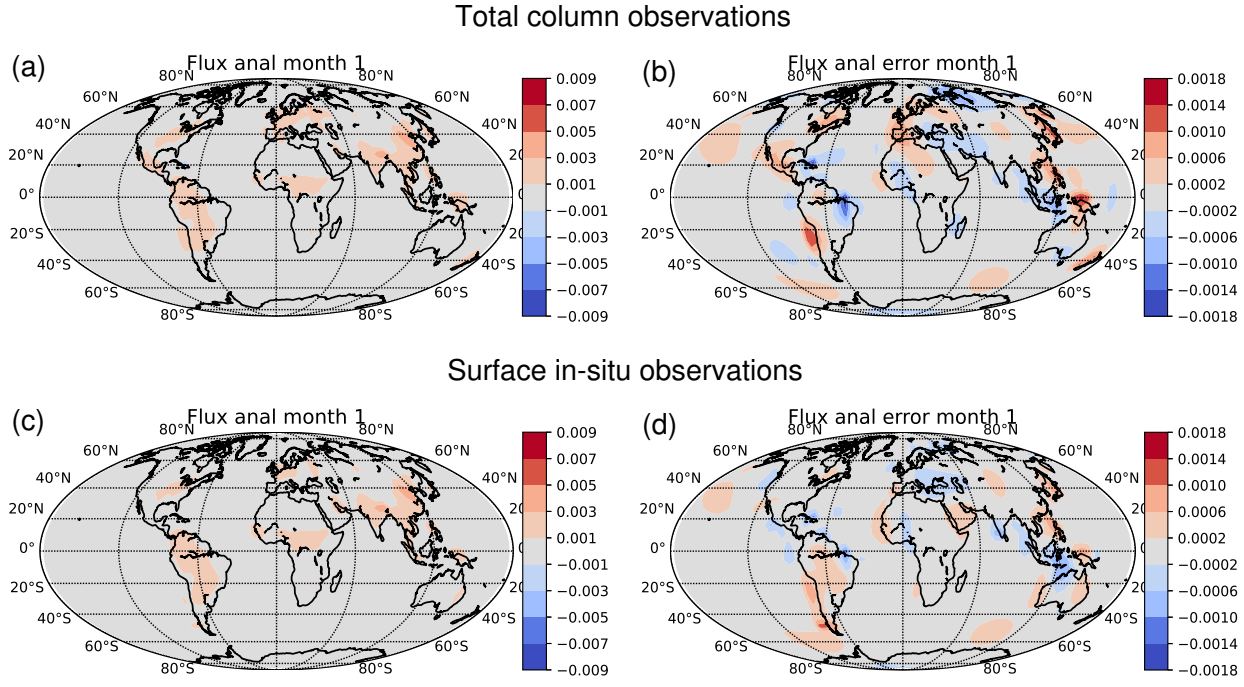

Figure 10. Analyses, $\rho^{\mathrm{a}}(0)$ (left column) and analysis errors (right column) for the quasi-real experiments (units $\mu\mathrm{g m}^{-2}\mathrm{s}^{-1}$). The top row is for TCA and the bottom row is for SIS observations.

The true state is shown in the top row of Fig. 9, $\chi^{\mathrm{t}}(0)$ (a) and $\rho^{\mathrm{t}}(0)$ (b). The distribution of flux shown is typical of methane, e.g. Meirink et al. (2006, 2008a); Qu et al. (2021), with sources over eastern China, northern India, Europe, equatorial Africa, north eastern US, and South America, but the values themselves are not real-world values. The a-priori state (bottom row) has been generated from the truth by adding noise consistent with the $\mathbf{B}$-matrix, as specified in the right hand column of Table 1. Most of the perturbations to the flux (d) are over land, due to the much larger background error standard deviations there than over sea. Some parts, such as over Eastern Asia, north east Africa, eastern USA/Canada, western South America, and eastern Australasia have background errors that represent anomalous sources; other parts, such as Alaska, Brazil, north western and south Africa, Greenland, and Indonesia have anomalous sinks. The tracer background (c) is only subtly different to the truth as background errors in the tracer have been assigned small values. A different set of random perturbations would have given rise to a different background error pattern, but with the same lengthscales and magnitudes.

5.1 Quasi-real-world situation: perfectly specified assimilation results

Figure 10 shows analyses and analysis errors when the specifications of the DA system are perfect (i.e. the correct background and observation errors, no model error, and no observation biases). The assimilation of TCA and SIS observations each effectively correct the background errors, panels (a) and (c). On the colour scale of the plots, it is not possible to see differences between these experiments, so the analysis errors, $\rho^{\mathrm{a}}(0) - \rho^{\mathrm{t}}(0)$ have been plotted in panels (b) and (d). The analysis errors

https://doi.org/10.5194/egusphere-2025-6352
Preprint. Discussion started: 10 March 2026

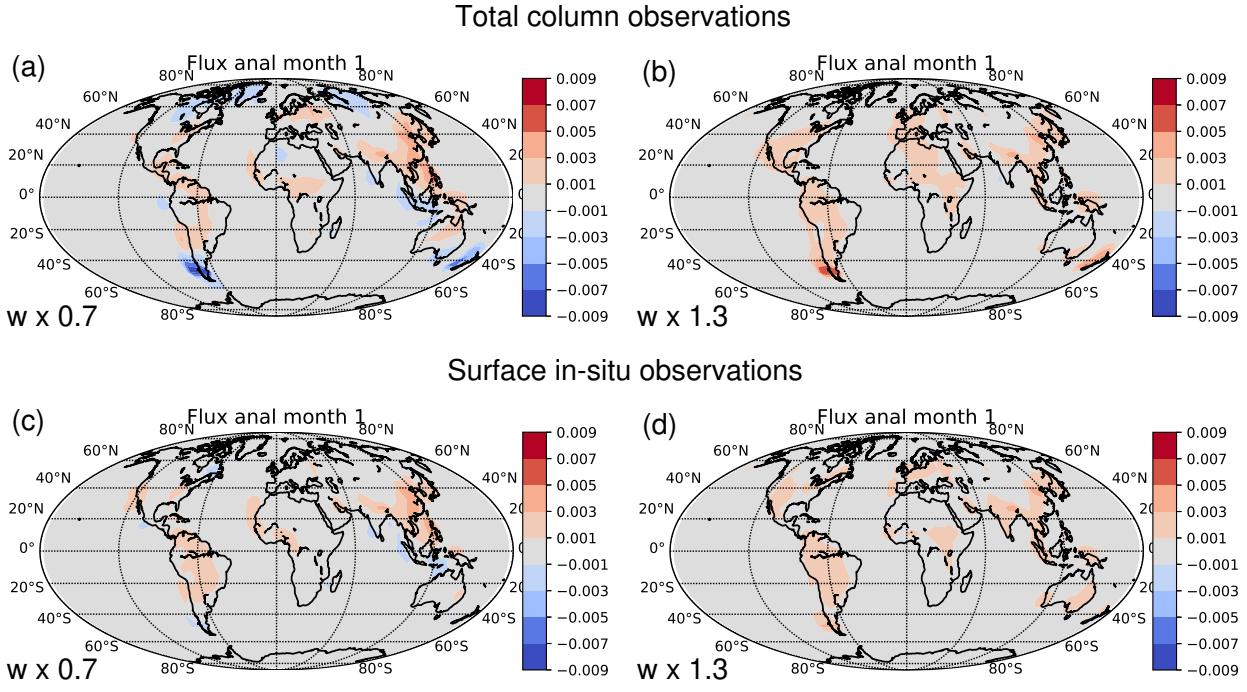

Figure 11. Analyses, $\rho^{\mathrm{a}}(0)$, for the quasi-real experiments found by assimilating either TCA (top row) or SIS observations (bottom row) for the case when a proxy for model error is applied in the assimilation. Model error is simulated by multiplying the vertical wind, w, used in the assimilation by either $\eta = 0.7$ (panels (a) and (c) or $\eta = 1.3$ (panels (b) and (d)). These plots should be compared to the true field in Fig. 9(b) (units $\mu\mathrm{g m}^{-2}\mathrm{s}^{-1}$).

following the assimilation of the different observation types are comparable, with the SIS observations leading (marginally) to the lower errors, consistent with the findings of Sect. 4.

5.2 Quasi-real-world situation: the effect of model error and observation bias

The effect of the model error proxy on these assimilation experiments is smaller than in the source/sink location experiments in Sect. 4. Figure 11 shows the effect of using $\eta = 0.7$ and 1.3 in the DA. Compared to the η values used in Fig. 6, values of η further from unity are required here to see noticeable effects in the analysis; this is probably because of the presence of the meaningful a-priori state here. The first point to note is that all experiments are still able to reduce the error from the background despite the presence of model error. Assimilating SIS observations is more robust against model error than for TCA observations, and it is hard to see differences on the colour scale between the bottom rows of Fig. 11 and Fig. 10(c). The most noticeable exception is for $\eta = 0.7$ in panel (c) where there is still some error in the sink field over Indonesia. This anomaly is also present for the $\eta = 0.7$ TCA experiment, panel (a), but exists together with anomalous sinks over Patagonia, New Zealand, north central Russia, north western Canada, and Greenland. Some of these anomalies (e.g. over Patagonia) are

https://doi.org/10.5194/egusphere-2025-6352
Preprint. Discussion started: 10 March 2026

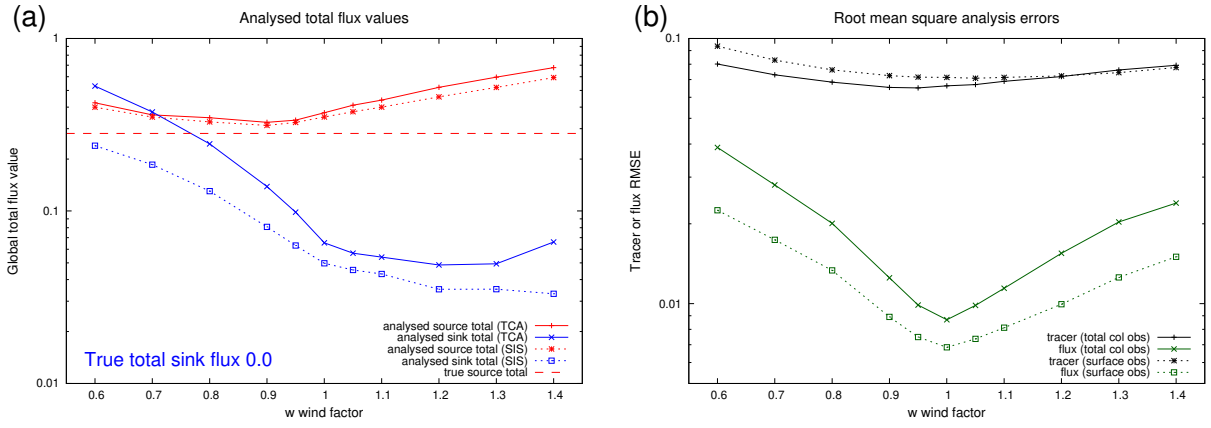

Figure 12. Summary of the effect of model error (via $w \rightarrow \eta w$) in the quasi-real assimilation experiments. Panel (a) shows the analysed global total source, $\int_{\rho^{\mathrm{a}}(0)>0} dA\rho^{\mathrm{a}}(0)$ (red lines), total sink, $\left|\int_{\rho^{\mathrm{a}}(0)<0} dA\rho^{\mathrm{a}}(0)\right|$ (blue lines) for the TCA (solid) and SIS (dotted) observation experiments. The true total source value is indicated by the dashed horizontal line (the true total sink is zero). Panel (b) shows the root mean square error in the analysed $\chi^{\mathrm{a}}(0)$ (black) and $\rho^{\mathrm{a}}(0)$ (green) for the TCA (solid) and SIS (dotted) observation experiments. The units are $\mathrm{Tg\,month}^{-1}$ for both panels.

not due to persistent background errors, but result from unaccounted for model error in the DA. The Patagonia anomaly changes sign from an anomalous sink for $\eta = 0.7$ in (a) to a source for $\eta = 1.3$ in (b).

5.3 Quasi-real-world situation: effect of model error on the on fluxes and analysis errors

A systematic analysis of the way that model error affects the total flux amounts is shown in Fig. 12(a) (TCA, solid lines; SIS dotted lines, truth dashed line; sources are red and sinks are blue). There is a general tendency of the analysed total fluxes to increase with η for both observation systems (this is straightforward to see for the sources for $\eta > 0.9$; in the case of the sinks, the absolute value decreases with η for $\eta < 1.2$, but the actual total sink is minus this value, which increases). This is consistent with the idea that, as the global circulation anomalously speeds up in the forward model used inside the DA (i.e. as η increases), tracer can no longer accumulate near the surface (where the SIS observations are located, and where the highest contribution to the TCA observations is made) and so higher emissions are required to compensate. As found in the flux location experiments (Sect. 4) and here, assimilating the SIS observations systematically gives results closer to the truth than for the TCA observations (this can be seen in panel (b) where the dotted red line (SIS) is closer to the dashed line (truth) than the solid red line (TCA), and the dotted blue line (SIS) is closer to zero (truth) than the solid blue line (TCA)).

Interestingly, this result appears to be the reverse of the findings of Basu et al. (2018), who found that TCA observations over land allowed more robust flux analyses than in situ observations. Their explanation concerned unaccounted for convective transport of tracer, which could affect in situ observations more than TCA observations. This is a compelling argument, but it may also be due to the different assigned error characteristics of each observation network.

https://doi.org/10.5194/egusphere-2025-6352
Preprint. Discussion started: 10 March 2026

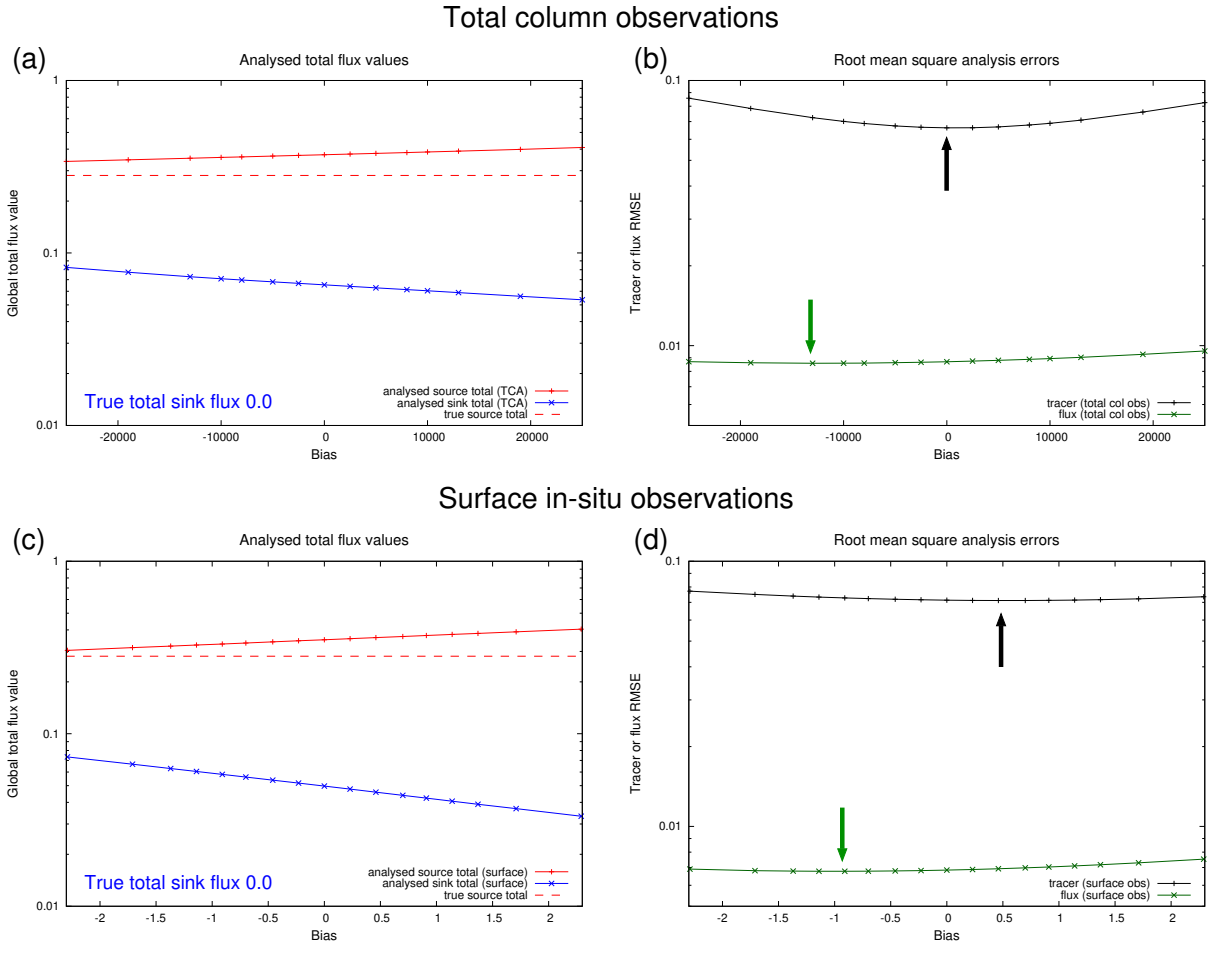

Figure 13. As Fig. 12 but varying observation bias. Panels (a) and (b) are for the TCA observations and (c) and (d) are for the SIS observations. The points with the smallest RMSE values are indicated with arrows.

The effect of model error on the root mean squared analysis errors (RMSEs) is quantified in Fig. 12(b). The RMSEs for flux (green lines) reassuringly minimise when $\eta = 1$ and are smaller for the assimilated SIS observations (dotted line) than for the TCA observations (solid), consistent with previous results. The finding is different for the RMSEs for the initial tracer (black lines). Here the experiment with the smallest RMSE for the TCA observation network is at $\eta = 0.95$ and for the SIS network is at $\eta = 1.05$. Further work would be required to decide if these deviations from $\eta = 1$ are due to the particular background or set of observations.

5.4 Quasi-real-world situation: effect of observation biases on the on fluxes and analysis errors

The final results in this demonstration study shows how the total flux amounts and analysis errors in the quasi-real-world situation vary with observation bias. We find that the presence of bias in this well-observed system does not change the pattern

https://doi.org/10.5194/egusphere-2025-6352
Preprint. Discussion started: 10 March 2026

of inferred fluxes from that of the unbiased observation system in the left panels of Fig. 10 (not shown), but does change the flux amounts.

A systematic analysis of the way that observation bias affects the total flux amounts is shown in Fig. 13 for TCA observations (a) and SIS observations (c), where solid lines are the analysed total fluxes (sources are red and sinks are blue), and the red dashed lines represent the true total source (the true total sink is zero in these experiments). The inferred total sources and sinks increase in value as the observation bias increases (the sinks need to be multiplied by -1 to find the actual sink values). This is the same conclusion as for the location experiments in Sect. 4.4. The absolute values of the total sources and sinks are overestimated in all experiments conducted, but as the amounts are found to increase with observation bias, the sources get further from the truth, but the sinks get closer to the truth (the true total sink is zero). This may not be a universal effect as it will probably change with different values of background error standard deviations. The effect on the TCA-observed system is larger than for the SIS-observed system. Recall that the observation biases are varied as a proportion of the random error up to $\pm$ just over half of σ^{o} for each observation type, so it is a broadly fair comparison between the two observation networks.

The RMSE analysis errors in 13(b) and (d) show minima at the observation bias values indicated with the arrows (these are added as an aid owing to the shallow curves on the logarithmic scale). With the exception of the black line in (b) (for $\chi^{\mathrm{a}}(0)$ errors for the TCA observations), the minima in the RMSEs do not align with zero bias. In the case of flux analysis errors, the "optimal" observation biases are negative. This has the effect of reducing the fluxes to values closer to the truth. This is an example of one type of error partially correcting for another (systematic biases compensating for the general overestimation of fluxes in the system), and can make the process of tuning such a DA system a complex task.

6 Summary, conclusions, and further work

This paper introduces a simplified tool, called EnviFlux, to allow investigations into inverse modelling techniques to infer surface fluxes. Such techniques have difficulties and shortcomings – mainly because of the indirectness of the observations in order to estimate surface flux information – and so there is always need for improvement. EnviFlux is designed as a base system to complement existing systems to allow basic experimentation cheaply without the need for high performance computing. The tool uses a semi-Lagrangian transport model, a spectrally modelled $\mathbf{B}$-matrix (which implies homogeneous background error correlations), and supports in situ tracer and flux, and total column amount observations. EnviFlux is a 4D-Var-based inverse model, which estimates the flux field on the same grid as the model, and it does this simultaneously with the initial tracer field. The tool can be used "as is" or can be expanded as required. The software is a suite of programs, mainly written in C++, with some python visualisation tools. Do to its intentional simplicity, there are some issues that EnviFlux cannot explore, such as those specific to satellite measurements (such as cloud and aerosol effects), and (currently) with unresolved transport, but it is designed to look at the general problem of extracting information from indirect observations.

EnviFlux is demonstrated in "weakly Bayesian" (where there is missing a-priori information, Sect. 4) and Bayesian (where the mean of the a-priori PDF is specified, Sect. 5) scenarios. The weakly Bayesian scenario comprises tests to infer the locations and strengths of a source/sink pair at (a-priori) unknown locations from a time sequence of observations of the tracer only. The

https://doi.org/10.5194/egusphere-2025-6352
Preprint. Discussion started: 10 March 2026

observation network comprises either total column amount (TCA) or surface in situ (SIS) observations, each following the path of a polar orbiting satellite. The former observation network is meant to resemble an actual instrument such as GOSAT, and the latter is a control for comparison. As long as there is no model error (see below) in the data assimilation, the system can successfully determine the locations of the flux features, but with peak values that are too small, and a spatial extent that is too large (the latter property is likely due to the particular lengthscales used to model the $\mathbf{B}$-matrix, and the fundamental smoothing effect of the inversion). A very simple proxy for model error is used by multiplying the vertical wind by a factor η in the inverse system, where $\eta = 1$ represents a perfect model. This first set of experiments is very sensitive to even small deviations of η from unity (e.g. 0.9 and 1.1), where the ability of the tool to infer even the correct locations of the flux features is compromised. Observation biases, however (in the ranges tested from $-0.57\sigma^{\text{o}}$ to $0.57\sigma^{\text{o}}$, where σ^{o} is the observation error standard deviation in each set of experiments – itself set to be 10% of the variability of the modelled observations in each case), do not affect the inferred locations, nor the peak values, but do affect the global total source and sink values. These results confirm other work that real-world inverse models need to have minimal imperfections in the forward model.

The Bayesian scenario (also referred to as the quasi-real-world case) uses similar observation networks, but uses methane-like spatial flux distributions as the observed true flux field. In the perfect model run, the choice of observation network has little effect on the ability of the assimilation to infer the correct qualitative structure of the true fluxes, but the in situ observations do offer advantages. Introducing model error gives rise to false sources and sinks. This becomes evident though at higher deviations from $\eta = 1$ than for the weakly Bayesian experiments, probably owing to the a-priori information available to the quasi-real case. Despite this, the assimilation still improves the flux estimates from the a-priori. Model error does also quantitatively change the total tracer released and absorbed and for most of the η values tested there is a tendency for the total sources and sinks to increase with η, which is may be due to the assimilation compensating for the faster transport of tracer in space away from the places where the observation operators are most sensitive. Separately, introducing observation bias in the same way as for the weakly Bayesian experiments, has the same effect on the total source and sink. By varying the bias, we find that the lowest RMSE analyses are not found for the experiments when the biases are zero (negative observation biases give the best results). A compelling argument for this is that it is compensating for the total analysed sources, which are too high in these experiments.

It is anticipated that this simplified system as a base can be used and developed further as a low-cost tool to test new ideas in inverse models for research projects and even for student projects. Some ideas and research questions that EnviFlux can contribute to are as follows. How sparse can the observation network be to infer detailed information on the location of new sources and sinks? How can EnviFlux be used to understand which observations contribute to which surface regions (e.g. by estimating the singular vectors of the forward model)? How well can an inverse model determine the timing of transient fluxes? How precise does the initial condition field need to be to effectively estimate fluxes, as this is needed to be precise or considered perfectly known (Bannister, 2011; Voshtani et al., 2023), and how long does an experiment have to run to virtually lose memory of the initial conditions? How is it possible to tune the background error covariances in real-world cases when they are not well known? How can model error be accounted for by developing techniques such as inflating the observation error variances (Lin and Gerbig, 2005; Chevallier et al., 2010; Houweling et al., 2010), or by including a model error term throughout

https://doi.org/10.5194/egusphere-2025-6352
Preprint. Discussion started: 10 March 2026

the atmosphere. How do different methods of estimating posterior error covariances compare, e.g. Lanczos or quasi-Newton-based, Meirink et al. (2008b); Niwa and Fujii (2020)? Can the system be used to test the ability of machine learning-based tools to emulate the forward part of the problem? By adding a simple chemical or land surface processes parametrisation, can the inversion be modified to estimate parameters in those models?

Code availability. The code will be made available via the Zenodo at https://doi.org/10.5281/zenodo.18018872 (Bannister, 2026).

Appendix A: The spectral transform

A1 The forward spectral transform

The forward spectral transform, $\mathbf{S}_\mathrm{h}$, is a key part of EnviFlux's covariance model. This transform acts on a vector which is a field increment in the spectral representation (i.e. a function of two integer wavenumbers l and m, see below). The output is a vector in the real space representation (i.e. a function of longitude, λ_i, and co-latitude, φ_j). Co-latitude is zero at the north pole, and so is related to latitude, ϕ, via $\varphi = 90 - \phi$. The basis functions of the spectral representation are the spherical harmonic functions, $Y_{lm}(\theta,\varphi)$:

$$Y_{lm}(\theta,\varphi) = \begin{cases} \bar{P}_{lm}(\cos\varphi)\cos(m\theta) & m \geq 0 \\ \bar{P}_{l|m|}(\cos\varphi)\sin(|m|\,\theta) & m < 0. \end{cases} \tag{A1}$$

Here $\bar{P}_{lm}$ are the associated Legendre polynomials (ALPs) of degree l and order m, and the bar notation on the $\bar{P}_{lm}$ indicates that they are "4π normalised" (other normalisations are possible). Let the representation in spectral space be v_{lm}, and in real space be x_{ij} (longitude θ_i, co-latitude φ_j). We have omitted the δ prefixes here for brevity. These are related via the following linear combination:

$$x_{ij} = \sum_{l=0}^{L} \sum_{m=-l}^{l} v_{lm} Y_{lm}(\theta_i,\varphi_j), \tag{A2}$$

where L is the chosen maximum degree. Equation (A2) is the mathematical form of the spectral transform. From the perspective of the transforms, the longitudes are best represented on a regularly spaced grid of $2L+1$ points, and the latitudes on a Gaussian grid of $L+1$ points (Errera and Ménard, 2012; Wieczorek et al., 2018). This is the grid structure assumed here and is used by EnviFlux. The Gaussian grid enables exact quadrature (known as Gauss-Legendre quadrature, see Appendix A1).

In order to translate (A2) onto a computer, specifically using standard libraries, we do some rewriting. Substituting (A1) into (A2), separating the l summation into $l = 0$ and $l > 0$ parts, and further separating the m summation into $-l \leq m \leq -1$,

https://doi.org/10.5194/egusphere-2025-6352
Preprint. Discussion started: 10 March 2026

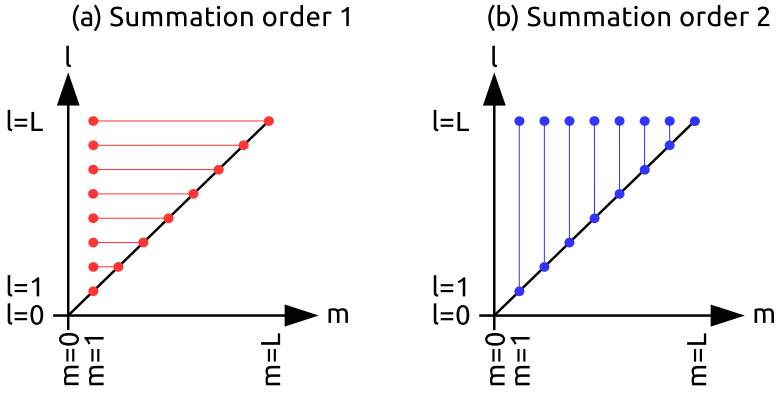

Figure A1. Orders of summations in m and l space as used in transforms (A3) and (A1). In order 1 (panel a), the sum over l is done first, and in order 2 (panel b), the sum over m is done first. Each order of summation is equivalent to the other as the same points are involved in the double summation.

$m = 0$, and $1 \le m \le l$ parts:

$$
\begin{aligned}
x_{ij} &= v_{00}\bar{P}_{00}(\cos\varphi_j) + \\
&\quad \sum_{l=1}^{L}\left[\sum_{m=-l}^{-1} v_{lm}\bar{P}_{l|m|}(\cos\varphi_j)\sin(|m|\,\theta_i) + \sum_{m=0}^{l} v_{lm}\bar{P}_{lm}(\cos\varphi_j)\cos(m\theta_i)\right] \\
&= v_{00}\bar{P}_{00}(\cos\varphi_j) + \\
&\quad \sum_{l=1}^{L}\left[\sum_{m=1}^{l} v_{l(-m)}\bar{P}_{lm}(\cos\varphi_j)\sin(m\theta_i) + v_{l0}\bar{P}_{l0}(\cos\varphi_j) + \sum_{m=1}^{l} v_{lm}\bar{P}_{lm}(\cos\varphi_j)\cos(m\theta_i)\right].
\end{aligned}
$$

The first and third terms can be combined, as can the second and fourth terms:

$$
x_{ij} = \sum_{l=0}^{L} v_{l0}\bar{P}_{l0}(\cos\varphi_j) + \sum_{l=1}^{L}\sum_{m=1}^{l} \bar{P}_{lm}(\cos\varphi_j)\left[v_{l(-m)}\sin(m\theta_i) + v_{lm}\cos(m\theta_i)\right].
$$

Further, let $v_{lm} = v_{lm}^{\mathrm{R}}$ $(0 \le m \le l)$, and $v_{l(-m)} = v_{lm}^{\mathrm{I}}$ $(1 \le m \le l)$:

$$
x_{ij} = \sum_{l=0}^{L} v_{l0}^{\mathrm{R}}\bar{P}_{l0}(\cos\varphi_j) + \sum_{l=1}^{L}\sum_{m=1}^{l} \bar{P}_{lm}(\cos\varphi_j)\left[v_{lm}^{\mathrm{R}}\cos(m\theta_i) + v_{lm}^{\mathrm{I}}\sin(m\theta_i)\right]. \tag{A3}
$$

This change of labelling means that we do not have to worry about negative wavenumber indices.

The double summation in Eq. (A3) first loops over l, and then loops over m where the upper m limit depends on l. This is summation order 1 in Fig. A1(a). In order to compute the above transform with standard software libraries, we first change the summations to the equivalent order 2 in Fig. A1(b):

$$
x_{ij} = \sum_{l=0}^{L} v_{l0}^{\mathrm{R}}\bar{P}_{l0}(\cos\varphi_j) + \sum_{m=1}^{L}\sum_{l=m}^{L} \bar{P}_{lm}(\cos\varphi_j)\left[v_{lm}^{\mathrm{R}}\cos(m\theta_i) + v_{lm}^{\mathrm{I}}\sin(m\theta_i)\right]. \tag{A1}
$$

https://doi.org/10.5194/egusphere-2025-6352
Preprint. Discussion started: 10 March 2026

This can then be split into a Legendre part and a Fourier part. First define the following:

$$\tilde{v}^{\mathrm{R}}_m(\cos\varphi_j) = \sum_{l=m}^{L} v^{\mathrm{R}}_{lm} \bar{P}_{lm}(\cos\varphi_j) \quad 0 \le m \le L \tag{A2a}$$

$$\tilde{v}^{\mathrm{I}}_m(\cos\varphi_j) = \sum_{l=m}^{L} v^{\mathrm{I}}_{lm} \bar{P}_{lm}(\cos\varphi_j) \quad 1 \le m \le L, \tag{A2b}$$

which leaves the rest of the transform as

$$x_{ij} = \tilde{v}^{\mathrm{R}}_0(\cos\varphi_j) + \sum_{m=1}^{L} \left[\tilde{v}^{\mathrm{R}}_m(\cos\varphi_j)\cos(m\theta_i) + \tilde{v}^{\mathrm{I}}_m(\cos\varphi_j)\sin(m\theta_i) \right]. \tag{A3}$$

The inputs to this spectral transform are the sets of coefficients in m,l-space v^{R}_{lm} ($0 \le m \le L$, $m \le l \le L$), and v^{I}_{lm} ($1 \le m \le L$, $m \le l \le L$). These are transformed to the intermediate sets of coefficients in m,j space, $\tilde{v}^{\mathrm{R}}_m(\cos\varphi_j)$ and $\tilde{v}^{\mathrm{I}}_m(\cos\varphi_j)$ using Eqs. (A2) (the "tilde" variables are half in spectral space, half in real space). In the code, these summations are performed explicitly using tables of ALPs pre-calculated from *SHTools* (Wieczorek et al., 2018). The spectral transform is completed to i,j space (complete real space) using the standard Fourier transform (A3), which is performed exactly by the routine *rfft1b* in the *fftpack* library (Swarztrauber et al., 2016). Note that in data assimilation work, the transform from spectral to real space is part of the *forward transform* (since it is part of the string of operators that go from control space to observation space, $\mathbf{HMB}^{1/2}$ in Eq. (5)), although readers may be more familiar with the transforms (A2) and (A3) being referred to an *inverse transforms*. This is an unfortunate clash of terminology.

A1 The inverse spectral transform

The inverse spectral transform, $\mathbf{S}_{\mathrm{h}}^{-1}$, changes the representation of a field increment from real space (a function of longitude, λ_i, and co-latitude, φ_j) to spectral space (a function of the degree, l, and order, m). The inverse of (A2) and (A3) is done in reverse order. Firstly, the $\tilde{v}^{\mathrm{R}}_m$ and $\tilde{v}^{\mathrm{I}}_m$ coefficients are found from standard Fourier transform formulae, which exploit the orthogonality of the sine and cosine functions:

$$\tilde{v}^{\mathrm{R}}_0(\cos\varphi_j) = \frac{1}{2L+1} \sum_{i=0}^{2L} x_{ij} \tag{A4a}$$

$$\tilde{v}^{\mathrm{R}}_m(\cos\varphi_j) = \frac{2}{2L+1} \sum_{i=0}^{2L} x_{ij} \cos m\theta_i \quad 1 \le m \le L \tag{A4b}$$

$$\tilde{v}^{\mathrm{I}}_m(\cos\varphi_j) = \frac{2}{2L+1} \sum_{i=0}^{2L} x_{ij} \sin m\theta_i \quad 1 \le m \le L. \tag{A4c}$$

https://doi.org/10.5194/egusphere-2025-6352
Preprint. Discussion started: 10 March 2026

This is the inverse of (A3) and is performed by the routine *rfft1f* in the *fftpack* library. Next the v^{R}_{lm} and v^{I}_{lm} (fully spectral) coefficients are found from the formulae (derived below):

$$v^{\mathrm{R}}_{l0} = \frac{1}{2}\sum_{j=0}^{L}\tilde{v}^{\mathrm{R}}_{0}(\cos\varphi_j)\bar{P}_{l0}(\cos\varphi_j)\mathrm{GaussWt}(\varphi_j) \quad 0\le l\le L \tag{A5a}$$

$$v^{\mathrm{R}}_{lm} = \frac{1}{4}\sum_{j=0}^{L}\tilde{v}^{\mathrm{R}}_{m}(\cos\varphi_j)\bar{P}_{lm}(\cos\varphi_j)\mathrm{GaussWt}(\varphi_j) \quad 1\le m\le L \quad m\le l\le L \tag{A5b}$$

$$v^{\mathrm{I}}_{lm} = \frac{1}{4}\sum_{j=0}^{L}\tilde{v}^{\mathrm{I}}_{m}(\cos\varphi_j)\bar{P}_{lm}(\cos\varphi_j)\mathrm{GaussWt}(\varphi_j) \quad 1\le m\le L \quad m\le l\le L, \tag{A5c}$$

where $\mathrm{GaussWt}(\varphi_j)$ are the Gaussian weights (GWs), which are found (together with the ALPs themselves) from the *SHtools* package. The make up the inverse of (A2). The GWs allow co-latitude integrals of the following type to be discretised when values $f(\varphi_j)$ are on Gaussian latitude points φ_j as shown:

$$\int_{\varphi=0}^{\pi} f(\varphi)\sin\varphi d\varphi = \sum_{j=0}^{L} f(\varphi_j)\mathrm{GaussWt}(\varphi_j). \tag{A6}$$

Equations (A5) are derived from (A2) via the following orthogonality property of ALPs:

$$\int_{\varphi=0}^{\pi} \bar{P}_{lm}(\cos\varphi)\bar{P}_{l'm}(\cos\varphi)\sin\varphi d\varphi = 2(2-\delta_{0m})\delta_{ll'}, \tag{A7}$$

which, using (A6), becomes

$$\sum_{j=0}^{L} \bar{P}_{lm}(\cos\varphi_j)\bar{P}_{l'm}(\cos\varphi_j)\mathrm{GaussWt}(\varphi_j) = 2(2-\delta_{0m})\delta_{ll'}. \tag{A8}$$

Multiplying (A2a) by $\bar{P}_{l'm}(\cos\varphi_j)\mathrm{GaussWt}(\varphi_j)$, summing over j, and then using (A8) gives

$$\begin{aligned}\sum_{j=0}^{L}\tilde{v}^{\mathrm{R}}_{m}(\cos\varphi_j)\bar{P}_{l'm}(\cos\varphi_j)\mathrm{GaussWt}(\varphi_j) &= \sum_{l=m}^{L} v^{\mathrm{R}}_{lm}\sum_{j=0}^{L}\bar{P}_{lm}(\cos\varphi_j)\bar{P}_{l'm}(\cos\varphi_j)\mathrm{GaussWt}(\varphi_j) \quad 0\le m\le L\\ &= 2(2-\delta_{0m})\sum_{l=m}^{L} v^{\mathrm{R}}_{lm}\delta_{ll'}\\ &= 2(2-\delta_{0m})v^{\mathrm{R}}_{l'm} \qquad \text{for } m\le l'\le L.\end{aligned}$$

When $m=0$ this gives (A5a) and when $1\le m\le L$ this gives (A5b). Now multiplying (A2b) by $\bar{P}_{l'm}(\cos\varphi_j)\mathrm{GaussWt}(\varphi_j)$, summing over j, and then using (A8) similarly gives

$$\begin{aligned}\sum_{j=0}^{L}\tilde{v}^{\mathrm{I}}_{m}(\cos\varphi_j)\bar{P}_{l'm}(\cos\varphi_j)\mathrm{GaussWt}(\varphi_j) &= \sum_{l=m}^{L} v^{\mathrm{I}}_{lm}\sum_{j=0}^{L}\bar{P}_{lm}(\cos\varphi_j)\bar{P}_{l'm}(\cos\varphi_j)\mathrm{GaussWt}(\varphi_j) \quad 1\le m\le L\\ &= 2(2-\delta_{0m})\sum_{l=m}^{L} v^{\mathrm{I}}_{lm}\delta_{ll'}\\ &= 2(2-\delta_{0m})v^{\mathrm{I}}_{l'm} \qquad \text{for } m\le l'\le L.\end{aligned}$$

https://doi.org/10.5194/egusphere-2025-6352
Preprint. Discussion started: 10 March 2026

The $m = 0$ case is of no interest, which leaves only the cases when $1 \leq m \leq L$, which gives (A5c).

A2 The adjoint spectral transform

The adjoint of the spectral transform (which is part of $\mathbf{B}^{\intercal/2}$) is needed to compute implied covariances ($\mathbf{B}^{1/2}\mathbf{B}^{\intercal/2}$) and the gradient of the cost function (6). Given that the adjoint operator is mathematically equivalent to the operator that propagates gradients (in the reverse direction to the forward counterparts), we use this equivalence as a means of deriving the adjoint versions of (A3) and (A2). Let variables with a hat represent gradients (of some unspecified function) with respect to that variable, namely $\hat{z} = \partial/\partial z$.

We will start with (A3), and look at the gradient with respect to each input component ($\tilde{v}_0^{\mathrm{R}}(\cos\varphi_j)$, $\tilde{v}_m^{\mathrm{R}}(\cos\varphi_j)$, and $\tilde{v}_m^{\mathrm{I}}(\cos\varphi_j)$), and exploit the chain rule in each case. The first input component of the forward transform (A3) is $\tilde{v}_0^{\mathrm{R}}(\cos\varphi_j)$. The gradient with respect to this variable, $\hat{\tilde{v}}_0^{\mathrm{R}}(\cos\varphi_j)$, is the output of the adjoint operation:

$$\hat{\tilde{\chi}}_0^{\mathrm{R}}(\cos\varphi_j) = \sum_{i=0}^{2L} \frac{\partial x_{ij}}{\partial \tilde{v}_0^{\mathrm{R}}(\cos\varphi_j)} \hat{x}_{ij} = \sum_{i=0}^{2L} \hat{x}_{ij}, \tag{A9}$$

where the partial derivative is found from (A3). The next group of input components to (A3) is $\tilde{v}_m^{\mathrm{R}}(\cos\varphi_j)$ ($1 \leq m \leq L$). The gradient with respect to this variable, $\hat{\tilde{v}}_m^{\mathrm{R}}(\cos\varphi_j)$, is another output of the adjoint operation and is calculated are a similar way:

$$\hat{\tilde{v}}_m^{\mathrm{R}}(\cos\varphi_j) \sum_{i=0}^{2L} \frac{\partial x_{ij}}{\partial \tilde{v}_m^{\mathrm{R}}(\cos\varphi_j)} \hat{x}_{ij} = \sum_{i=0}^{2L} \cos(m\theta_i)\hat{x}_{ij} \quad m \leq l \leq L. \tag{A10}$$

The final group of input components is $\tilde{v}_m^{\mathrm{I}}(\cos\varphi_j)$ ($1 \leq m \leq L$) and are calculated in a similar way:

$$\hat{\tilde{v}}_m^{\mathrm{I}}(\cos\varphi_j) \sum_{i=0}^{2L} \frac{\partial x_{ij}}{\partial \tilde{v}_m^{\mathrm{I}}(\cos\varphi_j)} \hat{x}_{ij} = \sum_{i=0}^{2L} \sin(m\theta_i)\hat{x}_{ij} \quad m \leq l \leq L. \tag{A11}$$

Notice that the adjoint operators (A9), (A10), and (A11) are similar to the inverse Fourier formulae (A4a), (A4b), and (A4c) respectively, but with no prefactors. This means that the *rfft1f* routine in the *fftpack* library can be used to perform the adjoint.

The next adjoint step is of (A2), and we will look at the gradient with respect to each input component (v_{lm}^{R} and v_{lm}^{I}). The first group of input components of the forward transform (A2) is v_{lm}^{R}:

$$\hat{v}_{lm}^{\mathrm{R}} = \sum_{j=0}^{L} \frac{\partial \tilde{v}_m^{\mathrm{R}}(\cos\varphi_j)}{\partial v_{lm}^{\mathrm{R}}} \hat{\tilde{v}}_m^{\mathrm{R}}(\cos\varphi_j) = \sum_{j=0}^{L} \bar{P}_{lm}(\cos\varphi_j)\hat{\tilde{v}}_m^{\mathrm{R}}(\cos\varphi_j) \quad 0 \leq m \leq L, \quad m \leq l \leq L. \tag{A12}$$

The final group of input components is v_{lm}^{I}:

$$\hat{v}_{lm}^{\mathrm{I}} = \sum_{j=0}^{L} \frac{\partial \tilde{v}_m^{\mathrm{I}}(\cos\varphi_j)}{\partial v_{lm}^{\mathrm{I}}} \hat{\tilde{v}}_m^{\mathrm{I}}(\cos\varphi_j) = \sum_{j=0}^{L} \bar{P}_{lm}(\cos\varphi_j)\hat{\tilde{v}}_m^{\mathrm{I}}(\cos\varphi_j) \quad 1 \leq m \leq L, \quad m \leq l \leq L. \tag{A13}$$

Notice that the adjoint operators (A12) and (A13) are similar to the inverse Legendre formulae (A5b) and (A5c) respectively, but with different scaling (specifically no prefactors and no Gaussian weights).

https://doi.org/10.5194/egusphere-2025-6352
Preprint. Discussion started: 10 March 2026

The above steps are needed to perform the adjoint of the spectral transform in terms of separate Fourier and Legendre steps. It is also possible to write the adjoint of the whole horizontal transform (A2) in one go:

$$\hat{v}_{lm} = \sum_{j=0}^{L} \sum_{i=0}^{2L} Y_{lm}(\theta_i, \varphi_j) \hat{x}_{ij} \quad 0 \le l \le L, \quad -l \le m \le l, \tag{A14}$$

which is useful for the calibration of the horizontal transform (Appendix C1).

Appendix B: The practical application of the operators in Eq. (8)

B1 Application of the horizontal transform

The initial condition (ic) part of the control vector for use with the upper left part of Eq. (8) is a field that is a function of l, m, and height z, $\delta\boldsymbol{\chi}(0)(l,m,z)$. The $\mathbf{R}_\mathrm{h}\mathbf{S}_\mathrm{h}\mathbf{\Lambda}_{\mathrm{h}\chi}^{1/2}$ part of the CVT does the following. Let the lth diagonal element of $\mathbf{\Lambda}_{\mathrm{h}\chi}^{1/2}$ be $\mathbf{\Lambda}_{\mathrm{h}\chi}^{1/2}(l)$. The action of $\mathbf{\Lambda}_{\mathrm{h}\chi}^{1/2}$ is to multiply $\delta\boldsymbol{\chi}(0)(l,m,z)$ by $\mathbf{\Lambda}_{\mathrm{h}c}^{1/2}(l)$. The resulting fields then pass through the $\mathbf{S}_\mathrm{h}$ operator (separately for each z) resulting in a function of λ, φ, z. $\mathbf{S}_\mathrm{h}$ outputs on a Gaussian grid with the meridional coordinate being co-latitude (see Appendix A1). $\mathbf{R}_\mathrm{h}$ translates the co-latitudes, φ, to latitudes, ϕ. In general applications the $\mathbf{R}_\mathrm{h}$ operator may be also used to interpolate from the Gaussian grid to a different grid. This is not necessary in EnviFlux as it uses a Gaussian grid.

The flux part of the control vector for use with the lower right part of Eq. (8) is a field that is a function of l, m, and time t, $\boldsymbol{\rho}(l,m,t)$. The $\mathbf{R}_\mathrm{h}\mathbf{S}_\mathrm{h}\mathbf{\Lambda}_{\mathrm{h}\rho}^{1/2}$ part of the CVT does a similar thing as for the initial conditions, apart from acting on each t separately, and so the result being a function of λ, ϕ, t.

B2 Application of the vertical transform

Following on from the horizontal and reconfiguration transforms for the ic fields, the vertical transform, $\mathbf{F}_{\mathrm{v}\chi}\mathbf{\Lambda}_{\mathrm{v}\chi}^{1/2}\mathbf{F}_{\mathrm{v}\chi}^\intercal$, acts on ic fields that are a function of λ, ϕ, z. $\mathbf{F}_{\mathrm{v}\chi}$ and $\mathbf{\Lambda}_{\mathrm{v}\chi}$ are each $n_z \times n_z$ matrices and $\mathbf{\Lambda}_{\mathrm{v}c}$ is diagonal. $\mathbf{F}_{\mathrm{v}\chi}^\intercal$ projects onto vertical modes (the eigenvectors), $\mathbf{\Lambda}_{\mathrm{v}\chi}^{1/2}$ scales the projections, and $\mathbf{F}_{\mathrm{v}\chi}$ projects from the vertical modes back to z. This is done for each horizontal position separately. In EnviFlux, $\mathbf{F}_{\mathrm{v}\chi}$ and $\mathbf{\Lambda}_{\mathrm{v}\chi}^{1/2}$ are independent of longitude and latitude. The output of the vertical transform is also a function of λ, ϕ, z.

B3 Application of the temporal transform

Following on from the horizontal and reconfiguration transforms for the flux fields, the temporal transform, $\mathbf{F}_{\mathrm{t}\rho}\mathbf{\Lambda}_{\mathrm{t}\rho}^{1/2}\mathbf{F}_{\mathrm{t}\rho}^\intercal$, acts on fields that are a function of λ, ϕ, t. $\mathbf{F}_{\mathrm{t}\rho}$ and $\mathbf{\Lambda}_{\mathrm{t}\rho}$ are each $(T+1) \times (T+1)$ matrices, and $\mathbf{\Lambda}_{\mathrm{t}\rho}$ is diagonal. $\mathbf{F}_{\mathrm{t}\rho}^\intercal$ projects onto temporal modes (the eigenvectors), $\mathbf{\Lambda}_{\mathrm{t}\rho}^{1/2}$ scales the projections, and $\mathbf{F}_{\mathrm{t}\rho}$ projects from the temporal modes back to t. This is done for each horizontal position separately. The $\mathbf{\Lambda}_{\mathrm{t}\rho}^{1/2}$ is the same for each horizontal position. The output of the temporal transform is also a function of λ, ϕ, t.

https://doi.org/10.5194/egusphere-2025-6352
Preprint. Discussion started: 10 March 2026

Appendix C: Determining the transform matrices

Equation (8) is the form of the spectral-based control variable transform. The objects to be determined are the following: $\mathbf{F}_{\mathrm{v}\chi}$, $\mathbf{\Lambda}_{\mathrm{v}\chi}$, $\mathbf{\Lambda}_{\mathrm{h}\chi}$, $\mathbf{F}_{\mathrm{t}\rho}$, $\mathbf{\Lambda}_{\mathrm{t}\rho}$, and $\mathbf{\Lambda}_{\mathrm{h}\rho}$. The calibration procedures for determining the above objects are described here.

C1 Determining the variance spectra of the horizontal transforms

The horizontal transforms for the ic and the flux fields are each described in the form $\mathbf{S}_{\mathrm{h}}\mathbf{\Lambda}_{\mathrm{h}}^{1/2}$, where $\mathbf{S}_{\mathrm{h}}$ is the spectral transform (spherical harmonics to longitude/co-latitude, Sect. A1), $\mathbf{\Lambda}_{\mathrm{h}}^{1/2} = \mathbf{\Lambda}_{\mathrm{h}\rho}^{1/2}$ for the ic, and $\mathbf{\Lambda}_{\mathrm{h}}^{1/2} = \mathbf{\Lambda}_{\mathrm{h}\rho}^{1/2}$ for the flux. This section describes how $\mathbf{\Lambda}_{\mathrm{h}}$ can be determined given a prescribed form of the horizontal correlations.

The implied correlation is found by $\mathbf{S}_{\mathrm{h}}\mathbf{\Lambda}_{\mathrm{h}}^{1/2}\left(\mathbf{S}_{\mathrm{h}}\mathbf{\Lambda}_{\mathrm{h}}^{1/2}\right)^{\mathsf{T}} = \mathbf{S}_{\mathrm{h}}\mathbf{\Lambda}_{\mathrm{h}}\mathbf{S}_{\mathrm{h}}^{\mathsf{T}}$. Using the spectral transform (A2) and the adjoint (A14), the result of acting with $\mathbf{S}_{\mathrm{h}}\mathbf{\Lambda}_{\mathrm{h}}\mathbf{S}_{\mathrm{h}}^{\mathrm{T}}$ on a field that is a function of longitude λ_i and co-latitude φ_j ($f(\lambda_i,\varphi_j)$), giving $f'(\lambda_{i'}\varphi_{j'})$ is

$$f'(\lambda_{i'}\varphi_{j'}) = \underbrace{\sum_{l=0}^{L}\sum_{m=-l}^{l} Y_{lm}(\theta_{i'},\varphi_{j'})}_{\mathbf{S}_{\mathrm{h}}}\underbrace{\mathbf{\Lambda}_{\mathrm{h}}(l,m)}_{\mathbf{\Lambda}_{\mathrm{h}}}\underbrace{\sum_{j=0}^{L}\sum_{i=0}^{2L} Y_{lm}(\theta_i,\varphi_j)}_{\mathbf{S}_{\mathrm{h}}^{\mathrm{T}}} f(\lambda_i,\varphi_j).$$

In this paper, $\mathbf{\Lambda}_{\mathrm{h}}$ is function of l only:

$$f'(\lambda_{i'}\varphi_{j'}) = \sum_{j=0}^{L}\sum_{i=0}^{2L}\sum_{l=0}^{L}\mathbf{\Lambda}_{\mathrm{h}}(l)\sum_{m=-l}^{l} Y_{lm}(\theta_{i'},\varphi_{j'})Y_{lm}(\theta_i,\varphi_j)f(\lambda_i,\varphi_j). \tag{C1}$$

The addition theorem of spherical harmonics (see e.g. Appendix A3, Eq. (A9) of Errera and Ménard (2012)) is

$$\sum_{m=-l}^{l} Y_{lm}(\theta_{i'},\varphi_{j'})Y_{lm}(\theta_i,\varphi_j) = \sqrt{2l+1}\bar{P}_{l0}(\cos\alpha), \tag{C2}$$

where α is the great circle angular separation between positions $(\theta_{i'},\varphi_{j'})$ and (θ_i,φ_j). Substituting (C2) into (C1) gives the convolution,

$$f'(\lambda_{i'}\varphi_{j'}) = \sum_{j=0}^{L}\sum_{i=0}^{2L}\underbrace{\sum_{l=0}^{L}\mathbf{\Lambda}_{\mathrm{h}}(l)\sqrt{2l+1}\bar{P}_{l0}(\cos\alpha)}_{\text{implied correlation matrix element}} f(\lambda_i,\varphi_j).$$

The implied correlation between $(\theta_{i'},\varphi_{j'})$ and (θ_i,φ_j) due to this horizontal transformation is the kernel indicated above:

$$C_{\mathrm{h}}(\lambda_{i'}\varphi_{j'};\lambda_i,\varphi_j) = C_{\mathrm{h}\alpha}(\alpha) = \sum_{l=0}^{L}\mathbf{\Lambda}_{\mathrm{h}}(l)\sqrt{2l+1}\bar{P}_{l0}(\cos\alpha). \tag{C3}$$

Notice that the right hand side is a function only of the separation between the two positions, α, and not on their individual values nor their relative orientation. These properties are called homogeneity and isotropy respectively. Let $C_{\mathrm{h}\alpha}(\alpha)$ be a prescribed function, e.g. the SOAR function $\{1+|d/\xi|\}\exp(-|d/\xi|)$, where $d = \alpha\pi R_{\mathrm{E}}/180$, α is in degrees, R_{E} is the

https://doi.org/10.5194/egusphere-2025-6352
Preprint. Discussion started: 10 March 2026

radius of the Earth, and ξ is the chosen lengthscale of the correlation (specified in the same units as $R_{\rm E}$). Multiply each side of (C3) by $\bar{P}_{l'0}(\cos\alpha)\sin\alpha$, and integrate over $\alpha = [0, \pi]$:

$$\int_{\alpha=0}^{\pi} C_{{\rm h}\alpha}(\alpha)\bar{P}_{l'0}(\cos\alpha)\sin\alpha = \sum_{l=0}^{L} \mathbf{\Lambda}_{\rm h}(l)\sqrt{2l+1} \int_{\alpha=0}^{\pi} \bar{P}_{l0}(\cos\alpha)\bar{P}_{l'0}(\cos\alpha)\sin\alpha.$$

The orthogonality property (A7) is then used:

$$\int_{\alpha=0}^{\pi} C_{{\rm h}\alpha}(\alpha)\bar{P}_{l'0}(\cos\alpha)\sin\alpha = \sum_{l=0}^{L} \mathbf{\Lambda}_{\rm h}(l)\sqrt{2l+1}\, 2\delta_{ll'} = 2\sqrt{2l'+1}\mathbf{\Lambda}_{\rm h}(l').$$

The horizontal variance spectrum is then given below in continuous form and then in discrete form using (A6):

$$\begin{aligned} \mathbf{\Lambda}_{\rm h}(l) &= \frac{1}{2\sqrt{2l+1}} \int_{\alpha=0}^{\pi} C_{{\rm h}\alpha}(\alpha)\bar{P}_{l0}(\cos\alpha)\sin\alpha \\ &= \frac{1}{2\sqrt{2l+1}} \sum_{j=0}^{L} C_{{\rm h}\alpha}(\alpha_j)\bar{P}_{l0}(\cos\alpha_j){\rm GaussWt}(\alpha_j). \end{aligned} \tag{C4}$$

It is important to ensure that $C_{{\rm h}\alpha}(0) = 1$ (which may not be true due to numerical errors in the above procedure). Once $\mathbf{\Lambda}_{\rm h}(l)$ is computed with (C4), $C_{{\rm h}\alpha}(0) = 1$ is ensured by multiplying $\mathbf{\Lambda}_{\rm h}(l)$ by $1/\left(\sum_{l=0}^{L} \mathbf{\Lambda}_{\rm h}(l)\sqrt{2l+1}\bar{P}_{l0}(1)\right)$.

C2 Determining the vertical transform for the initial concentration

The vertical transform is described by the $n_z \times n_z$ matrices $\mathbf{F}_{{\rm v}\chi}$ and $\mathbf{\Lambda}_{{\rm v}\chi}$ (see bullet point 2 of Sect. 3.3.1), where n_z is the number of vertical levels. In principle, there can be a different set of such vertical matrices for each horizontal position. For simplicity, we use just one set of eigenvectors (in $\mathbf{F}_{{\rm v}\chi}$) and eigenvalues (in $\mathbf{\Lambda}_{{\rm v}\chi}$), found from a global vertical correlation matrix (Fig. 3).

The correlation matrices are formed from 10 years (1995-2004) of twice-monthly methane forecasts, first detrended to correct for methane trends (even though there was little methane growth over this period, Rigby et al. (2008)).

C3 Determining the temporal transform for the flux

The temporal transform is described by the $(T+1) \times (T+1)$ matrices $\mathbf{F}_{{\rm t}\rho}$ and $\mathbf{\Lambda}_{{\rm t}\rho}$ (see bullet point 5 of Sect. 3.3.2). First a $(T+1) \times (T+1)$ correlation matrix $\mathbf{C}^{\rm t}$ is formed with matrix elements determined from a SOAR function, $\mathbf{C}^{\rm t}_{ij} = \{1 + |t_i - t_j|/\tau\}\exp(-|t_i - t_j|/\tau)$, where t_i and t_j are times (in months), and τ is the timescale. $\mathbf{F}_{{\rm t}\rho}$ and $\mathbf{\Lambda}_{{\rm t}\rho}$ are, respectively, eigenvectors and eigenvalues of $\mathbf{C}^{\rm t}$.

Appendix D: List of the software tools

The following is a list of the main modules available as part of the EnviFlux software. More details are documented in the user guide (Bannister, 2026).

https://doi.org/10.5194/egusphere-2025-6352
Preprint. Discussion started: 10 March 2026

- **Calibration.f90** Constructs a control variable transform file required for the system to run.
- **Master_MakeWinds.cpp** Makes suitable wind files from ERA5 winds to the format and resolution of EnviFlux. These drive the transport of the chosen tracer.
- **Master_MakeFields.cpp** Generates initial conditions and surface flux fields for a run of the forward model.
- **Master_Invicat2EnviFlux.cpp** Converts data from an INVICAT file to an EnviFlux file.
- **Master_ReplaceFirstField.cpp** Makes a copy of an EnviFlux file, but replacing the initial conditions from another file.
- **Master_GenerateObs.cpp** Outputs model observations from a given EnviFlux file.
- **Master_MakeBG.cpp** makes a background state by perturbing a specified truth with a random perturbation.
- **Master_Assimilate.cpp** runs 4DVar using a covariance file, a background file, and some observations to produce an analysis.
- **Master_CalcError.cpp** calculates the difference metrics between two states.

The following is a list of auxiliary modules to test some of the system components.

- **Master_TestReadWrite.cpp** Tests reading and writing of state and wind data.
- **Master_ForwardTraj.cpp** Computes the trajectory of a particle advected by the prescribed winds. This is for testing the trajectory code before it is used in the semi-Lagrangian advection scheme.
- **Master_AdjointTests_CVT.cpp** Tests the adjoints of the control variable transform components.
- **Master_AdjointTestsObObs.cpp** Tests the adjoint of the observation operators.
- **Master_AdjointTests_SemiLagrangian.cpp** Tests the adjoint of the semi-Lagrangian advection scheme.
- **Master_AdjointTests_SL+ObsOp.cpp** Tests the adjoint of the combined semi-Lagrangian advection scheme and the observation operator.
- **Master_ImpliedCov.cpp** Tests the control variable transform to give some implied covariances.
- **Master_GradTest.cpp** Tests the gradient produced by the penalty-and-gradient routine in EnviFlux.

The following is an example Python program to process and visualise the output of EnviFlux.

- **Plot_PriorPostInc.py** Takes information from a control variable transform file, observation files, truth, background, and analysis files to produce histograms, scatter plots, and diagnostic fields.

https://doi.org/10.5194/egusphere-2025-6352
Preprint. Discussion started: 10 March 2026

Author contributions. The author wrote the EnviFlux code, designed and ran the experiments, and wrote the paper.

Competing interests. The author declares no competing interests.

Acknowledgements. The author is grateful for financial support from the NERC National Centre for Earth Observation (contract number PR140015), and computing facilities from the University of Reading. The author acknowledges helpful correspondence with Chris Wilson (Univ. of Leeds) and Amos Lawless (Univ. of Reading).

https://doi.org/10.5194/egusphere-2025-6352
Preprint. Discussion started: 10 March 2026

References

Agustí-Panareda, A., Diamantakis, M., Massart, S., Chevallier, F., Muñoz-Sabater, J., Barré, J., Curcoll, R., Engelen, R., Langerock, B., Law, R. M., et al.: Modelling CO2 weather–why horizontal resolution matters, Atmospheric Chemistry and Physics, 19, 7347–7376, https://doi.org/10.5194/acp-19-7347-2019, 2019.

An, X., Henne, S., Yao, B., Vollmer, M. K., Zhou, L., and Li, Y.: Estimating emissions of HCFC-22 and CFC-11 in China by atmospheric observations and inverse modeling, Science China Chemistry, 55, 2233–2241, 2012.

Bannister, R. N.: A review of forecast error covariance statistics in atmospheric variational data assimilation. I: Characteristics and measurements of forecast error covariances, Quarterly Journal of the Royal Meteorological Society, 134, 1951–1970, https://doi.org/10.1002/qj.339, 2008a.

Bannister, R. N.: A review of forecast error covariance statistics in atmospheric variational data assimilation. II: Modelling the forecast error covariance statistics, Quarterly Journal of the Royal Meteorological Society, 134, 1971–1996, 2008b.

Bannister, R. N.: Issues in the assimilation of the sources of a trace gas by inverse modelling, Computers & Fluids, 46, 106–112, 2011.

Bannister, R. N.: The ABC-DA system (v1.4): a variational data assimilation system for convective scale assimilation research with a study of the impact of a balance constraint, Geoscientific Model Development, 13, 3789–3816, https://doi.org/10.5194/gmd-13-3789-2020, 2020.

Bannister, R. N.: EnviFlux techincal and user guide, and code respository, https://doi.org/10.5281/zenodo.18803399, 2026.

Basu, S., Baker, D. F., Chevallier, F., Patra, P. K., Liu, J., and Miller, J. B.: The impact of transport model differences on CO2 surface flux estimates from OCO-2 retrievals of column average CO2, Atmospheric Chemistry and Physics, 18, 7189–7215, https://doi.org/10.5194/acp-18-7189-2018, 2018.

Bey, I., Jacob, D. J., Yantosca, R. M., Logan, J. A., Field, B. D., Fiore, A. M., Li, Q., Liu, H. Y., Mickley, L. J., and Schultz, M. G.: Global modeling of tropospheric chemistry with assimilated meteorology: Model description and evaluation, Journal of Geophysical Research: Atmospheres, 106, 23 073–23 095, https://doi.org/10.1029/2001JD000807, 2001.

Bisht, J. S., Patra, P. K., Takigawa, M., Sekiya, T., Kanaya, Y., Saitoh, N., and Miyazaki, K.: Estimation of CH4 emission based on an advanced 4D-LETKF assimilation system, Geoscientific Model Development, 16, 1823–1838, https://doi.org/10.5194/gmd-16-1823-2023, 2023.

Chandra, N., Patra, P. K., Niwa, Y., Ito, A., Iida, Y., Goto, D., Morimoto, S., Kondo, M., Takigawa, M., Hajima, T., et al.: Estimated regional CO2 flux and uncertainty based on an ensemble of atmospheric CO2 inversions, Atmospheric Chemistry and Physics, 22, 9215–9243, https://doi.org/10.5194/acp-22-9215-2022, 2022.

Chen, H. W., Zhang, F., Lauvaux, T., Davis, K. J., Feng, S., Butler, M. P., and Alley, R. B.: Characterization of regional-scale CO2 transport uncertainties in an ensemble with flow-dependent transport errors, Geophysical Research Letters, 46, 4049–4058, https://doi.org/10.1029/2018GL081341, 2019.

Chevallier, F., Engelen, R. J., and Peylin, P.: The contribution of AIRS data to the estimation of CO2 sources and sinks, Geophysical research letters, 32, 2005a.

Chevallier, F., Fisher, M., Peylin, P., Serrar, S., Bousquet, P., Bréon, F.-M., Chédin, A., and Ciais, P.: Inferring CO2 sources and sinks from satellite observations: Method and application to TOVS data, Journal of Geophysical Research: Atmospheres, 110, https://doi.org/10.1029/2005JD006390, 2005b.

Chevallier, F., Bréon, F.-M., and Rayner, P. J.: Contribution of the Orbiting Carbon Observatory to the estimation of CO2 sources and sinks: Theoretical study in a variational data assimilation framework, Journal of Geophysical Research: Atmospheres, 112, 2007.

https://doi.org/10.5194/egusphere-2025-6352
Preprint. Discussion started: 10 March 2026

Chevallier, F., Feng, L., Bösch, H., Palmer, P. I., and Rayner, P. J.: On the impact of transport model errors for the estimation of CO2 surface fluxes from GOSAT observations, Geophysical Research Letters, 37, 1–5, 2010.

Chipperfield, M.: New version of the TOMCAT/SLIMCAT off-line chemical transport model: Intercomparison of stratospheric tracer experiments, Quarterly Journal of the Royal Meteorological Society: A journal of the atmospheric sciences, applied meteorology and physical oceanography, 132, 1179–1203, 2006.

Errera, Q. and Ménard, R.: Spectral representation of spatial correlations in variational assimilation with grid point models and application to the Belgian Assimilation System for Chemical Observations (BASCOE), Atmospheric Chemistry and Physics, 12, 10 015–10 031, 2012.

Feng, L., Palmer, P., Bösch, H., and Dance, S.: Estimating surface CO2 fluxes from space-borne CO2 dry air mole fraction observations using an ensemble Kalman Filter, Atmospheric Chemistry and Physics, 9, 2619–2633, 2009.

Fraser, A., Palmer, P., Feng, L., Boesch, H., Cogan, A., Parker, R., Dlugokencky, E., Fraser, P., Krummel, P., Langenfelds, R., et al.: Estimating regional methane surface fluxes: the relative importance of surface and GOSAT mole fraction measurements, Atmospheric Chemistry and Physics, 13, 5697–5713, 2013.

Golub, G. H. and Van Loan, C. F.: Matrix computations. 1996, Johns Hopkins University, Press, Baltimore, MD, USA, pp. 374–426, 1996.

Gonzi, S., Palmer, P. I., Barkley, M. P., De Smedt, I., and van Roozendael, M.: Biomass burning emission estimates inferred from satellite column measurements of HCHO: Sensitivity to co-emitted aerosol and injection height, Geophysical Research Letters, 38, 2011.

Grell, G. A., Peckham, S. E., Schmitz, R., McKeen, S. A., Frost, G., Skamarock, W. C., and Eder, B.: Fully coupled "online" chemistry within the WRF model, Atmospheric environment, 39, 6957–6975, https://doi.org/10.1016/j.atmosenv.2005.04.027, 2005.

Gurney, K. R., Law, R. M., Denning, A. S., Rayner, P. J., Baker, D., Bousquet, P., Bruhwiler, L., Chen, Y.-H., Ciais, P., Fan, S., et al.: Towards robust regional estimates of CO2 sources and sinks using atmospheric transport models, Nature, 415, 626–630, 2002.

Henze, D. K., Hakami, A., and Seinfeld, J. H.: Development of the adjoint of GEOS-Chem, Atmospheric Chemistry and Physics, 7, 2413–2433, https://doi.org/10.5194/acp-7-2413-2007, 2007.

Hirsch, A., Michalak, A., Bruhwiler, L., Peters, W., Dlugokencky, E., and Tans, P.: Inverse modeling estimates of the global nitrous oxide surface flux from 1998–2001, Global Biogeochemical Cycles, 20, 2006.

Hodyss, D. and Nichols, N.: The error of representation: Basic understanding, Tellus A: Dynamic Meteorology and Oceanography, 67, 24 822, 2015.

Hourdin, F. and Armengaud, A.: Test of a hierarchy of finite-volume schemes for transport of trace species in an atmospheric general circulation model, Mon. Wea. Rev, 127, 822–837, https://doi.org/10.1175/1520-0493(1999)127<0822:TUOFVM>2.0.CO;2, 1999.

Houweling, S., Kaminski, T., Dentener, F., Lelieveld, J., and Heimann, M.: Inverse modeling of methane sources and sinks using the adjoint of a global transport model, Journal of Geophysical Research: Atmospheres, 104, 26 137–26 160, 1999.

Houweling, S., Aben, I., Breon, F.-M., Chevallier, F., Deutscher, N., Engelen, R., Gerbig, C., Griffith, D., Hungershoefer, K., Macatangay, R., et al.: The importance of transport model uncertainties for the estimation of CO2 sources and sinks using satellite measurements, Atmospheric chemistry and physics, 10, 9981–9992, https://doi.org/10.5194/acp-10-9981-2010, 2010.

Houweling, S., Bergamaschi, P., Chevallier, F., Heimann, M., Kaminski, T., Krol, M., Michalak, A. M., and Patra, P.: Global inverse modeling of CH4 sources and sinks: an overview of methods, Atmospheric chemistry and physics, 17, 235–256, https://doi.org/10.5194/acp-17-235-2017, 2017.

Hu, Y., Li, Y., Ma, X., Liang, Y., You, W., Pan, X., and Zang, Z.: The optimization of SO2 emissions by the 4DVAR and EnKF methods and its application in WRF-Chem, Science of The Total Environment, 888, 163 796, https://doi.org/10.1016/j.scitotenv.2023.163796, 2023.

https://doi.org/10.5194/egusphere-2025-6352
Preprint. Discussion started: 10 March 2026

Jiang, Z., Jones, D. B., Worden, H. M., Deeter, M. N., Henze, D. K., Worden, J., Bowman, K. W., Brenninkmeijer, C., and Schuck, T.: Impact of model errors in convective transport on CO source estimates inferred from MOPITT CO retrievals, Journal of Geophysical Research: Atmospheres, 118, 2073–2083, 2013.

Krol, M., Houweling, S., Bregman, B., Van den Broek, M., Segers, A., Van Velthoven, P., Peters, W., Dentener, F., and Bergamaschi, P.: The two-way nested global chemistry-transport zoom model TM5: algorithm and applications, Atmospheric Chemistry and Physics, 5, 417–432, 2005.

Lewis, J. M., Lakshmivarahan, S., and Dhall, S.: Dynamic data assimilation: a least squares approach, vol. 13, Cambridge University Press, 2006.

Lin, J. and Gerbig, C.: Accounting for the effect of transport errors on tracer inversions, Geophysical Research Letters, 32, 2005.

Lunt, M. F., Palmer, P. I., Feng, L., Taylor, C. M., Boesch, H., and Parker, R. J.: An increase in methane emissions from tropical Africa between 2010 and 2016 inferred from satellite data, Atmospheric Chemistry and Physics, 19, 14 721–14 740, 2019.

Ma, J., Kooijmans, L. M., Cho, A., Montzka, S. A., Glatthor, N., Worden, J. R., Kuai, L., Atlas, E. L., and Krol, M. C.: Inverse modelling of carbonyl sulfide: implementation, evaluation and implications for the global budget, Atmospheric Chemistry and Physics, 21, 3507–3529, 2021.

Meirink, J., Eskes, H., and Goede, A.: Sensitivity analysis of methane emissions derived from SCIAMACHY observations through inverse modelling, Atmospheric Chemistry and Physics, 6, 1275–1292, 2006.

Meirink, J. F., Bergamaschi, P., Frankenberg, C., d'Amelio, M. T., Dlugokencky, E. J., Gatti, L. V., Houweling, S., Miller, J. B., Röckmann, T., Villani, M. G., et al.: Four-dimensional variational data assimilation for inverse modeling of atmospheric methane emissions: Analysis of SCIAMACHY observations, Journal of Geophysical Research: Atmospheres, 113, 2008a.

Meirink, J. F., Bergamaschi, P., and Krol, M. C.: Four-dimensional variational data assimilation for inverse modelling of atmospheric methane emissions: method and comparison with synthesis inversion, Atmospheric chemistry and physics, 8, 6341–6353, 2008b.

Munassar, S., Monteil, G., Scholze, M., Karstens, U., Rödenbeck, C., Koch, F.-T., Totsche, K. U., and Gerbig, C.: Why do inverse models disagree? A case study with two European CO2 inversions, Atmospheric Chemistry and Physics, 23, 2813–2828, https://doi.org/10.5194/acp-23-2813-2023, 2023.

Niwa, Y. and Fujii, Y.: A conjugate BFGS method for accurate estimation of a posterior error covariance matrix in a linear inverse problem, Quarterly Journal of the Royal Meteorological Society, 146, 3118–3143, https://doi.org/10.1002/qj.3838, 2020.

Palmer, P. I., Jacob, D. J., Jones, D., Heald, C. L., Yantosca, R. M., Logan, J. A., Sachse, G. W., and Streets, D. G.: Inverting for emissions of carbon monoxide from Asia using aircraft observations over the western Pacific, Journal of Geophysical Research: Atmospheres, 108, 2003.

Palmer, P. I., Abbot, D. S., Fu, T.-M., Jacob, D. J., Chance, K., Kurosu, T. P., Guenther, A., Wiedinmyer, C., Stanton, J. C., Pilling, M. J., et al.: Quantifying the seasonal and interannual variability of North American isoprene emissions using satellite observations of the formaldehyde column, Journal of Geophysical Research: Atmospheres, 111, https://doi.org/10.1029/2005JD006689, 2006.

Pendergrass, D. C., Jacob, D. J., Nesser, H., Varon, D. J., Sulprizio, M., Miyazaki, K., and Bowman, K. W.: CHEEREIO 1.0: a versatile and user-friendly ensemble-based chemical data assimilation and emissions inversion platform for the GEOS-Chem chemical transport model, Geoscientific Model Development, 16, 4793–4810, https://doi.org/10.5194/gmd-16-4793-2023, 2023.

Press, W., Teukolsky, S., Vetterling, W., and Flannery, B.: Numerical Recipes 3rd Edition: The Art of Scientific Computing, Cambridge University Press, Cambridge, UK, 2007.

https://doi.org/10.5194/egusphere-2025-6352
Preprint. Discussion started: 10 March 2026

Qu, Z., Jacob, D. J., Shen, L., Lu, X., Zhang, Y., Scarpelli, T. R., Nesser, H., Sulprizio, M. P., Maasakkers, J. D., Bloom, A. A., et al.: Global distribution of methane emissions: a comparative inverse analysis of observations from the TROPOMI and GOSAT satellite instruments, Atmospheric Chemistry and Physics, 21, 14 159–14 175, https://doi.org/10.5194/acp-21-14159-2021, 2021.

Rigby, M., Prinn, R. G., Fraser, P. J., Simmonds, P. G., Langenfelds, R., Huang, J., Cunnold, D. M., Steele, L. P., Krummel, P. B., Weiss, R. F., et al.: Renewed growth of atmospheric methane, Geophysical research letters, 35, 2008.

Rodgers, C. D.: Inverse methods for atmospheric sounding: theory and practice, vol. 2, World scientific, 2000.

Schuh, A. E., Jacobson, A. R., Basu, S., Weir, B., Baker, D., Bowman, K., Chevallier, F., Crowell, S., Davis, K. J., Deng, F., et al.: Quantifying the impact of atmospheric transport uncertainty on CO2 surface flux estimates, Global Biogeochemical Cycles, 33, 484–500, https://doi.org/10.1029/2018GB006086, 2019.

Swarztrauber, P., Valent, R., and Burkardt, J.: FFTPack module for Fortran, https://github.com/keurfonluu/FFTPack/blob/master/src/fftpack5.f90, online; accessed 31-January-2023, 2016.

Thompson, R. L., Lassaletta, L., Patra, P. K., Wilson, C., Wells, K. C., Gressent, A., Koffi, E. N., Chipperfield, M. P., Winiwarter, W., Davidson, E. A., et al.: Acceleration of global N2O emissions seen from two decades of atmospheric inversion, Nature Climate Change, 9, 993–998, https://doi.org/doi.org/10.1038/s41558-019-0613-7, 2019.

Voshtani, S., Ménard, R., Walker, T. W., and Hakami, A.: Use of assimilation analysis in 4D-Var source inversion: Observing System Simulation Experiments (OSSEs) with GOSAT methane and hemispheric CMAQ, Atmosphere, 14, 758, https://doi.org/10.3390/atmos14040758, 2023.

Wieczorek, M. A., Meschede, M., Sales de Andrade, E., Oshchepkov, I., Xu, B., Leinweber, K., and Walker, A.: SHTOOLS: Version 4.4, https://doi.org/10.5281/zenodo.2350781, online; accessed 25-January-2023, 2018.

Wilson, C., Chipperfield, M., Gloor, M., and Chevallier, F.: Development of a variational flux inversion system (INVICAT v1. 0) using the TOMCAT chemical transport model, Geoscientific Model Development, 7, 2485–2500, https://doi.org/10.5194/gmd-7-2485-2014, 2014.

Yokota, T., Yoshida, Y., Eguchi, N., Ota, Y., Tanaka, T., Watanabe, H., and Maksyutov, S.: Global concentrations of CO2 and CH4 retrieved from GOSAT: First preliminary results, Sola, 5, 160–163, https://doi.org/10.2151/sola.2009-041, 2009.

Yu, X., Millet, D. B., and Henze, D. K.: How well can inverse analyses of high-resolution satellite data resolve heterogeneous methane fluxes? Observing system simulation experiments with the GEOS-Chem adjoint model (v35), Geoscientific Model Development, 14, 7775–7793, https://doi.org/10.5194/gmd-14-7775-2021, 2021.

Zhuravlev, R., Ganshin, A., Maksyutov, S. S., Oshchepkov, S., and Khattatov, B.: Estimation of global CO2 fluxes using ground-based and satellite (GOSAT) observation data with empirical orthogonal functions, Atmospheric and Oceanic Optics, 26, 507–516, https://doi.org/10.1134/S1024856013060158, 2013.